NASA/CR—1999-209170

Bubble Generation in a Continuous Liquid Flow Under Reduced Gravity Conditions

Salvatore Cezar Pais
Case Western Reserve University, Cleveland, Ohio

July 1999

The NASA STI Program Office . . . in Profile

Since its founding, NASA has been dedicated to the advancement of aeronautics and space science. The NASA Scientific and Technical Information (STI) Program Office plays a key part in helping NASA maintain this important role.

The NASA STI Program Office is operated by Langley Research Center, the Lead Center for NASA's scientific and technical information. The NASA STI Program Office provides access to the NASA STI Database, the largest collection of aeronautical and space science STI in the world. The Program Office is also NASA's institutional mechanism for disseminating the results of its research and development activities. These results are published by NASA in the NASA STI Report Series, which includes the following report types:

- TECHNICAL PUBLICATION. Reports of completed research or a major significant phase of research that present the results of NASA programs and include extensive data or theoretical analysis. Includes compilations of significant scientific and technical data and information deemed to be of continuing reference value. NASA's counterpart of peer-reviewed formal professional papers but has less stringent limitations on manuscript length and extent of graphic presentations.

- TECHNICAL MEMORANDUM. Scientific and technical findings that are preliminary or of specialized interest, e.g., quick release reports, working papers, and bibliographies that contain minimal annotation. Does not contain extensive analysis.

- CONTRACTOR REPORT. Scientific and technical findings by NASA-sponsored contractors and grantees.

- CONFERENCE PUBLICATION. Collected papers from scientific and technical conferences, symposia, seminars, or other meetings sponsored or cosponsored by NASA.

- SPECIAL PUBLICATION. Scientific, technical, or historical information from NASA programs, projects, and missions, often concerned with subjects having substantial public interest.

- TECHNICAL TRANSLATION. English-language translations of foreign scientific and technical material pertinent to NASA's mission.

Specialized services that complement the STI Program Office's diverse offerings include creating custom thesauri, building customized data bases, organizing and publishing research results . . . even providing videos.

For more information about the NASA STI Program Office, see the following:

- Access the NASA STI Program Home Page at ***http://www.sti.nasa.gov***

- E-mail your question via the Internet to help@sti.nasa.gov

- Fax your question to the NASA Access Help Desk at (301) 621-0134

- Telephone the NASA Access Help Desk at (301) 621-0390

- Write to:
  NASA Access Help Desk
  NASA Center for AeroSpace Information
  7121 Standard Drive
  Hanover, MD 21076

NASA/CR—1999-209170

Bubble Generation in a Continuous Liquid Flow Under Reduced Gravity Conditions

Salvatore Cezar Pais
Case Western Reserve University, Cleveland, Ohio

Prepared under Grant NGT5–1168

National Aeronautics and
Space Administration

Glenn Research Center

July 1999

Acknowledgments

I wish to express my thanks and deep gratitude to my dissertation advisors, Professor Yasuhiro Kamotani and Professor Simon Ostrach for their patience, encouragement, guidance and unwavering support they have given me through out this work. I am greatly indebted to them for the unswerving support they have given me for all these years. Their numerous suggestions have made this work possible. The interaction I have had with them for these past years has given me the confidence necessary to tackle numerous problems. Without their help and guidance I would not have been in this position. Thank you.

I am also thankful to Mr. John B. McQuillen and Dr. Bhim Singh of NASA Glenn Research Center, for all their help with the parabolic flight experiments. The physical suffering that I endured during these flights has its merits. My thanks also go to Mr. Bud Vance and Mr. Mike Dobbs for their technical support. The DC-9 crew, especially Mr. John Yaniec and Mr. Eric Neumann were especially kind to me, and helped me at some crucial moments. Thank you.

I also wish to thank my colleagues for their patience and cooperation. Many thanks are due to Mr. A. Bhunia, Dr. J.P. Kizito, Dr. J. Masud, Dr. F.B. Weng, and Ms. L. Wang. The efforts of Mr. A. Bhunia in helping me with the theoretical analysis are highly appreciated. I thank Dr. Jehanzeb Masud for his patience in helping me edit the thesis document. Thanks are also due to Kevin Stultz, Mike Anderson and to Dr. John Kizito for their help with video image digitization.

Finally, I wish to gratefully acknowledge the financial help I have received from the National Aeronautics and Space Administration as a NASA Research Fellow under grant (NGT5–1168).

Available from

NASA Center for Aerospace Information
7121 Standard Drive
Hanover, MD 21076
Price Code: A08

National Technical Information Service
5285 Port Royal Road
Springfield, VA 22100
Price Code: A08

TABLE OF CONTENTS

LIST OF TABLES AND FIGURES

NOMENCLATURE

Symbols

A_{eff}	Effective cross-sectional bubble area acted upon by liquid drag
Bo_P	Bond number ($Weber_P$ / $Froude_P$)
C_D	Drag coefficient of a bubble moving through an infinite expanse
C_{DW}	Coefficient of drag with respect to the flow conduit wall
C_{MC}	Added mass coefficient (function of non-dim. bubble diameter)
D_B	Dimensional bubble diameter
D_B^*	Non-dimensional bubble diameter (D_B / D_P)
D_P	Flow conduit pipe inner diameter
D_N	Gas injection nozzle diameter
D_N^*	Non-dimensional gas injection nozzle diameter (D_N / D_P)
Fr_P	Froude number $[(\rho_c-\rho_d)U_{LS}^2 / \rho_c g D_P]$
F_B	Buoyancy force
F_D	Liquid drag force
F_I	Inertia force
F_M	Gas momentum flux
F_R	Reference force ($\rho_c U_{LS}^2 D_P^2$)
F_σ	Surface tension force
L_N (En)	Bubble neck length

L_R Reference length (D_P)

Re_P Reynolds number based on pipe diameter ($\rho_c U_{LS} D_P / \mu_c$)

Re_B Reynolds number based on bubble diameter ($\rho_c U_{eff} D_B / \mu_c$)

Q_c Volumetric liquid flow rate

Q_d Volumetric gas flow rate

t_R Reference time (D_P / U_{LS})

U_{eff} [(ds/dt) - U_{LS}]

U_{GS} Superficial gas velocity

U_{GS}^* Non-dimensional superficial gas velocity

U_{LS} Superficial liquid velocity

V_B Bubble volume

We_P Weber number ($\rho_c U_{LS}^2 D_P / \sigma_c$)

Y Distance from bubble center to gas injection nozzle tip

ds/dt bubble center velocity away from the gas injection nozzle tip

Greek Symbols

ε Void fraction

Δ Dist. bet. fronts of detached and previously detached bubbles

ρ_c Liquid density

ρ_d Gas density

μ_c , μ_d Liquid and gas absolute viscosities

CHAPTER 1

INTRODUCTION

The development of two-phase flow research under reduced gravity conditions is prompted by space applications such as thermal energy generation and transport ,as well as the design and development of long duration life support systems.

With the advent of programs dealing with manned exploration of space, as well as the possible near term construction of an International Space Station, two-phase flow studies under microgravity conditions become imperative. Commercialization of results obtained from such research will broaden the scope of microgravity programs as indicated by Ostrach (1988). Consequently, it is highly feasible that terrestrial industries stand to profit from exploiting this new knowledge basis.

Situations where a gas and a liquid flow together in a pipe occur often on Earth, some examples, being refrigerators, oil and gas pipelines, nuclear powerplants and water desalination facilities (Hewitt, 1996 and Hill, 1997). In the presence of gravity, there is a tendency for the gas and liquid phases to separate due to their different densities, with liquids descending and gases

rising. This phenomenon is not observed under reduced gravity conditions. Eventhough, many experiments have been performed to examine gas-liquid flows on Terra, there is still a lack of understanding of the observed phenomena, thus rendering accurate prediction of such flows quite difficult, if not downright intractable.

Besides the benefit of improved understanding of Earth-based two-phase flows, reduced gravity gas-liquid flows are studied for possible use in space; in particular for design of two-phase thermal control systems, to replace pumped liquid loops, currently in use for the design and operation of a thermal bus intended for the Space Station. This thermal management system is designed to function as the primary heat sink aboard the Station.

In a gas-liquid thermal control system used aboard spacecraft, liquid warms and boils (becoming vapor) as it is heated, while the vapor cools and condenses (becoming liquid), as the heat is dissipated through the radiators. The main advantage of this system is its reduced weight, since it requires a smaller volume of liquid than an all liquid system. Subsequently, a smaller volume of liquid at a lower flow rate can be used since large amounts of energy are transferred in boiling and condensation. With the reintroduction of

the Shuttle-C program, any weight saving for payload transfer to orbit is of utmost importance.

Furthermore, heat transfer associated with space-based nuclear powerplants, be they located in orbit, on reduced gravity extra-terrestrial soil, or aboard spacecraft, is highly dependent on two-phase flow research under reduced and microgravity conditions. Such studies can prevent emergencies associated with unanticipated loss of coolant, which can result in catastrophe. For space-based thermal management systems, an alternative to using heat pipes for transporting thermal energy is to utilize capillary pumped loops (Herold and Kolos, 1997). This device provides heat rejection at a wider range of temperatures and avoids counterflows of liquid and vapor typically found in heat pipes.

Another useful space application is transport of cryogens, such as liquid oxygen and liquid nitrogen, which vaporize to some extent as they flow through pipes or into storage tanks, thereby creating gas-liquid flows. In particular, the design of propulsion and life support systems stands to benefit from this application.

Last but not least, the study of gas-liquid flows under reduced gravity conditions can yield results which can be adapted to improving design of equipment used in both terrestrial and microgravity applications.

Since gas-liquid flows in a reduced gravity environment are considered as simpler to analyze than those under normal gravity conditions, there is increased interest from NASA's Microgravity Science Program, resulting in studies which simulate reduced gravity using both drop towers and aircraft flying parabolic trajectories, such as the KC-135 and the DC-9 Reduced Gravity Aircraft.

Under normal gravity conditions, bubble generation is usually accomplished by injecting gas through an orifice into a quiescent liquid medium. Due to the buoyancy force created by the Earth's gravitational field, the bubble grows and detaches quite readily.

On the other hand, under reduced gravity conditions, the role that the buoyancy force plays upon bubble growth and consequent detachment, is significantly diminished. Thus, in a reduced gravity environment larger and more spherical bubbles can be obtained. Since the role of buoyancy is minimized, another bubble detaching force is required in order to control bubble size and frequency of generation. Hypothetically speaking, an

electrostatic, temperature or acoustic field can create the necessary conditions for bubble detachment. In view of all these possibilities, the most practical solution to the problem at hand is to use the drag force provided by liquid flowing through the two-phase flow conduit, as pointed out by Chuang and Goldschmidt (1970) and more recently by Kim et al. (1994).

Two configurations generally used for bubble dispersion in a flowing liquid are the co-flow and the cross-flow geometries. In the co-flow configuration, the dispersed phase is introduced through a nozzle in the same direction with the liquid flow; whereas in the cross-flow geometry, gas is injected perpendicular to the direction of liquid flow.

Independent of flow system configuration, under both normal and reduced gravity conditions, there exist three major flow patterns which occur with increasing gas injection rate, namely bubble, slug (Taylor bubble) and annular (Jayawardena et al., 1997). Bubble and annular flows are mostly used in space-based two-phase systems. Due to vibrations caused by slugs, which result in unwanted accelerations, determining the correct flow pattern is imperative for efficient operation of such systems.

Bubble generation due to gas injection can be divided into three conditions, namely constant flow, constant pressure and intermediate conditions (Kumar and Kuloor, 1970). At constant flow conditions, studied in this thesis, the volumetric gas flow rate remains constant throughout the bubble formation process. Depending on the gas flux, there are three known regimes of bubble generation, namely the static, dynamic and turbulent regimes. The static regime occurs at very low flow rates, typically smaller than 1 cm^3/s (Van Krevelen and Hoftijzer, 1950), whereas high gas flow rate corresponds to the turbulent regime. For industrial applications and hence of utmost practical importance, is the dynamic regime which covers the range of gas injection rates from 1 cm^3/s to 10^4 cm^3/s for an air-water system (Wraith, 1971).

The dynamic regime can further be divided into two subregimes, such as single bubble (including pairing) and double bubble (McCann and Prince, 1971). In the single bubble subregime, which occurs at low gas flow rates, uniformly spaced bubbles of approximately, equal size are produced. Depending on the gravity level, these bubbles can be spherical or can deviate from the spherical shape. At higher gas flow rates, namely in the double bubble subregime, two bubbles can coalesce at the nozzle exit. With increasing gas flux, bubble coalescence becomes more frequent, in time

forming a gas jet and thereby leading to a transition from the dynamic to the turbulent regime.

The present reduced gravity work focuses on single bubble formation and presents an experimentally observed mechanism for the onset condition of coalescence. Under reduced and microgravity conditions, a single bubble can grow larger than the pipe diameter before detachment occurs, thereby giving rise to a Taylor bubble. A Taylor bubble can also be formed by coalescence of two smaller bubbles at the gas injection nozzle interface. The inception of a Taylor bubble characterizes the transition from bubbly to slug flow, which has been extensively studied by Duckler et al. (1988), Colin et. al. (1991), Bousman et. al. (1996) and more recently by Jayawardena et.al. (1997). These investigators performed several two-phase flow experiments under reduced gravity conditions, to allow for high speed measurement of void fraction, liquid film thickness and pressure drop. They found that flow pattern occurrence is influenced by liquid and gas superficial velocities, tube diameter, liquid viscosity and surface tension.

Bubble generation by nozzle injection in a quiescent liquid has been extensively studied in the past. A compendium of pertinent literature is presented by Rabiger and Vogelpohl (1986) as well as by Tsuge (1986).

More recently, Pamperin and Rath (1995) investigated the influence of buoyancy on bubble formation from submerged orifices by performing drop tower experiments. They showed that under reduced gravity conditions the bubble diameter is directly proportional to the gas injection orifice diameter and also that the size of generated bubbles tends to increase with increasing gas injection rate.

Along the same lines, Buyevich and Webbon (1996) concluded that the buoyancy force and the gas momentum flux are critical detaching forces for bubble generation in a quiescent liquid. They observed that under normal gravity conditions, the bubble growth and detachment process is dominated by buoyancy while under reduced gravity conditions, in the abscence of a cross-flow, or a co-flow of liquid, this process is primarily influenced by the gas momentum flux. Hence, at normal and moderately reduced gravity conditions, as the gas flow rate is increased, bubble formation frequency slightly decreases and the detaching bubble grows in size.

Mori and Baines (1997) studied bubble growth by gas diffusion from a nucleation site on a solid horizontal surface in a quiescent liquid under normal gravity conditions. They performed experiments using carbon dioxide gas bubbles formed in water and showed that evolution of bubble shape

during growth, as a direct result of gas injection rate, is important for determining departure size. It was shown that growing bubbles form a neck at the bubble base before detachment occurs. As this neck pinches off, the remaining section of the bubble collapses into the nucleation cavity, directly affecting the growth rate of subsequent bubbles.

Since under reduced gravity conditions, the gas momentum flux presents the sole bubble detaching mechanism, this fact necessitates the presence of another detaching force to control bubble size and frequency of generation. This force can be provided by using a co-flow or a cross-flow system. Bubble formation in the cross-flow configuration has been extensively studied by Al-Hayes and Winterton (1981), Kawase and Ulbrecht (1981) and Kim et al. (1994). More recently, Nahra and Kamotani (1997), showed that bubble size decreases with increasing superficial liquid velocity, while the bubble time to detachment also decreases as the liquid flow rate is increased, This observation stresses the role of liquid flow as a detaching force in the bubble formation process.

Oguz et al. performed a set of microgravity experiments in order to study the effect of a cross-flow on a bubble injected from a hole located in the flow conduit wall. This situation is of primary interest for two-phase flow studies as

they relate to heat transfer. The experimental apparatus was installed in a drop tower bus module and subjected to a series of free fall tests. They concluded that under the influence of a cross-flow, bubble detachment is triggered by bubble deformation due to the combined effect of viscous liquid drag and inertia forces.

Furthermore, vapor bubble departure in convective boiling, which displays the cross-flow geometry, has been extensively studied by Zeng et al. (1993). They show that forces acting on the growing bubble include the surface tension force, the quasi-steady liquid drag, the unsteady drag due to asymmetrical bubble growth, the shear lift force, the buoyancy force, the hydrodynamic pressure force and the contact pressure force.

Despite its practical significance, the co-flow configuration has not been as extensively studied as the cross-flow geometry. Kim(1992) proposed a theoretical model for bubble generation in a co-flowing liquid under normal and reduced gravity conditions. His work is an extension of a model proposed by Chuang and Goldschmidt (1970).

Sada et al. (1978) performed normal gravity experiments in order to observe the effect liquid velocity has on bubble detachment in a co-flow configuration. They reported a decrease in bubble size with increasing liquid flow rate.

More recently, Oguz et al. (1996) reported some preliminary results of air bubble formation via single nozzle gas injection in a terrestrial vertical upflow configuration. By keeping air flow rate constant, and increasing the water flow rate, they observed a substantial reduction in bubble volume with increasing liquid volumetric flow rate. This physical phenomenon is also experimentally observed in Bhunia et al. (1998), for bubble generation via single nozzle gas injection within a liquid co-flow configuration in a reduced gravity environment.

Under microgravity or reduced gravity conditions, bubble generation and resulting two-phase flow by multiple nozzle injection along the periphery of the flow conduit has been studied by several investigators. A summary of this work, covering the topic of bubble and slug flow at microgravity conditions, addressing state of knowledge and open questions pertaining to this subject, is presented by Colin et al. (1996).

With multiple nozzle injection along the periphery of the flow conduit, due to coalescence of adjacent bubbles, it is quite difficult to control the uniformity of

generated bubble size. A better alternative is controlled bubble generation via single nozzle injection, which is the experimental method used in the present work.

The work at hand is an experimental investigation of bubble generation by gas injection through a single nozzle in a co-flow and cross-flow system. Experiments using air as the dispersed phase and water as the continuous phase were performed in parabolic flight aboard the DC-9 Reduced Gravity Research Aircraft at NASA Lewis Research Center.

The main objective of the current investigation is the study of bubble formation in liquid flow within a pipe, via a single nozzle gas injection system. Particularly, we are interested in bubble size and frequency of generation as well as resulting two-phase flow (primarily bubbly and transition to slug flow regimes).

It was experimentally observed that with increasing superficial liquid velocity, generated bubbles decreased in size, holding all other flow conditions constant. The bubble diameter was shown to increase by increasing the ratio of gas injection nozzle diameter to pipe diameter and also detached bubbles grew in size with increasing pipe diameter. Likewise, it was shown that bubble frequency of formation increased, and hence the time to detachment

of a forming bubble decreased, as the superficial liquid velocity was increased.

Furthermore, it is observed that void fraction can be accurately controlled with single nozzle gas injection by simply varying the volumetric gas and liquid flow rates.

A theoretical model was developed based on previous work, for the co-flow configuration, considering two stages for bubble generation, namely the expansion stage and the detachment stage (Ramakrishnan et al., 1969 and Kim, 1994. The present numerical work is valid in the bubbly flow regime and predicts bubble diameter up to the transition point to slug flow (formation of Taylor bubbles). Based on an overall force balance, which incorporates forces such as buoyancy, surface tension acting at the nozzle exit, gas momentum flux, liquid drag, liquid inertia and bubble inertia, and acts at the two stages of bubble generation, the detached bubble diameter is computed. Under reduced gravity conditions, the role of the buoyancy force is diminished but is not overlooked.

Computational results agree well with current reduced gravity data. The detachment criteria is checked against the experimental data and proved valid at low superficial liquid velocity. At higher superficial liquid velocities, as the bubble neck length begins to deviate greatly from the value of the air

injection nozzle diameter, experimental bubble size no longer matches the theoretical prediction. Effects of fluid properties, injection geometry and flow conditions (such as Reynolds number, Weber number and Froude number, all based on pipe diameter) on resulting bubble size are numerically investigated.

CHAPTER 2

Experimental Work

2.1 Reduced Gravity Aircraft Facilities

Experiments were conducted aboard the DC-9 Reduced Gravity Research Aircraft at the NASA Lewis Research Center. Other reduced gravity aircraft, currently in use are the Learjet Model 25 and the KC-135 aircraft based at the NASA Johnson Space Center. These flight platforms were not used in our currently reported experiments.

In general, these microgravity research aircraft achieve weightlessness by flying a parabolic trajectory. The number of parabolic trajectories executed per flight mission varies.

The Learjet aircraft can perform a maximum of six trajectories per flight, while both the KC-135 and the DC-9 aircraft can typically achieve 40 to 50 trajectories in a single mission. However, due to aircraft configuration as well as chosen flight trajectory, the KC-135, similar to the Learjet aircraft, provides a rougher ride than the DC-9 aircraft.

Usually these reduced gravity aircraft can perform up to two flights a day, unless grounding is necessary due to an onboard malfunction. Gravity levels of 0.02g (reduced gravity), .17g (lunar), and .33g (Martian) can be produced by modifying the flight trajectory. Without resorting to space flight, the parabolic flight technique currently produces the longest period of reduced gravity, exceeding drop tower experiment run times by 10 to 15 seconds. It is true that drop towers offer lower gravity levels than parabolic flight, however major physical phenomena vary slightly by reducing the gravity level below 0.01g.

The DC-9 aircraft is capable of performing an average of 45 low-gravity maneuvers per flight. A typical flight mission duration, including take-off and landing, is two to three hours. Each parabolic trajectory lasts for approximately 18 to 22 seconds. Only 5 to 10 seconds are available for free-float experiments, which experience a 10^{-3}g to 10^{-4}g environment. Since the experiments we performed were attached to the aircraft floor the maximum time period of 22 seconds was available for operational purposes. Out of this time period, data was acquired for 15 seconds.

After the aircraft initially reaches 18,000-20,000 feet above the ground, it initiates its 2g pull-up. The aircraft continues to move at a constant air speed

of 400 mph, while climbing another 7000 feet to reach the apex of its flight trajectory.

During a typical flight trajectory, the aircraft is pitched up in a pull-up maneuver until a 55^0 to 60^0 nose-up attitude is reached. As the aircraft slows toward the apex of the parabolic trace, its nose is pitched down. Consequently, when the aircraft reaches a 35^0 to 40^0 nose-down attitude, it is pitched back up to level flight or into the next parabolic trajectory. The brief pushover, which results as the DC-9 traces the apex of the parabolic path, produces less than 1 percent of terrestrial gravity for approximately 20 seconds.

When executed properly, the pull-up and pullout maneuvers generate accelerations on the aircraft of up to two times the Earth's gravitational accelerations.

The modified DC-9 is also capable of flying modified parabolic trajectories in order to provide intermediate acceleration levels ranging from 0.1g to 0.75g. In order to monitor the quality of the reduced gravity environment, existent during flight aboard the DC-9, three-axis accelerometers accurate to 0.001g were mounted within the aircraft. A typical time trace of the z-axis (floor to ceiling) acceleration level measured during a reduced gravity trajectory, has a mean value of 0.008g with a standard deviation of 0.017 g, in the time period

of 7 to 18 seconds when the aircraft was experiencing reduced gravity conditions. Minor oscillations observed in this trace were caused by trajectory corrections, atmospheric turbulence and aircraft structural vibrations.

Since all acceleration levels acting on the aircraft were actively controlled by two pilots, similar results were generated for the x-axis (nose to tail) and y-axis (wing tip to wing tip) accelerations. For the experimental tests reported in this investigation, only data acquired when recorded acceleration was within 0.02g of zero in all three directions, is presented. As a direct consequence, typical duration of these experiments was 9 to 17 seconds.

2.2 Test Sections

Two distinct test section geometries were used in our experiments, namely the co-flow and the cross-flow configurations. Dry and filtered air was used as the dispersed phase while distilled water acted as the continuous phase.

Figure 1 displays the co-flow system. In this configuration, air was injected in the same direction with the water flow. The test section consists of a Plexiglas pipe which acts as the two phase flow conduit. A tee branch fitting is mounted on the inlet side of the pipe using a Swagelock fitting. Air was

injected through a stainless steel tube, whose converging orifice tip had been welded on. This welded section facilitates the use of various gas injection nozzle diameter holes, which can be drilled into a small section of stainless steel stock. The tube acts as a nozzle and protrudes into the transparent pipe, clearing the hydrodynamic entrance length, respective of pipe diameter. In other words, protrusion of the air-injection nozzle well within the pipe, ensures that the bubble is injected in a region where the surrounding liquid flow is hydrodinamically fully developed. The liquid and gas mixing region within the pipe, in view of the video camera, was surrounded by a Plexiglas rectangular box filled with distilled water.

The role of this viewing box is to avoid image distortion caused by the difference in refractive indices of the curved surface of the two-phase flow conduit and the surrounding air medium. This box presents a flat surface to the video camera. The enclosed space between the viewing box and the test section was filled with water, because the refractive index of Plexiglas is closer to the refractive index of water than to that of air. Distilled water which acts as the continuous phase, was introduced through the remaining port of the tee branch fitting.

On the other hand, in the cross-flow configuration air was injected perpendicular to the direction of water flow. This test section, shown in figure 2, was machined out of a rectangular piece of Plexiglas stock into the form of a tee-section. Two orthogonally positioned, equal diameter holes were bored into the Plexiglas tee. Through one of these holes air was injected via a stainless steel tube whose converging orifice tip was welded on. The other hole, which was bored the whole way through the Plexiglas tee, acts as the two phase flow conduit as well as the water inlet tube. For this configuration, there was no need for a viewing box, since the curved portion of the flow conduit was not directly exposed to the video camera but was rather enclosed by a flat Plexiglas surface

The co-flow and cross-flow test sections were mounted in series in the manner shown in figure 3. This was primarily the most efficient manner of obtaining the maximum amount of data per flight, by simply interchanging the air flow tube connector between the co-flow and cross-flow test sections. The complete test section assembly was integrated within the Learjet Two Phase Flow Apparatus, developed by McQuillen and Neumann (1995).

For every experimental run, a new batch of distilled water was used in order to minimize contamination at the bubble surface as much as possible. No surfactants were added to the distilled water reservoir.

2.3 Test Flow Loop Layout

The Two-Phase Flow Apparatus consists of three distinct sections. Two of these structures are standard racks which have been designed for use aboard the Learjet Model 25 Reduced Gravity Aircraft. The third rack, introduced between the two standard ones, was custom designed to fit user needs.

All three racks were equipped with electrical and plumbing connections for power and flow control. There was an additional electrical connection between the two standard racks for the purpose of data acquisition.

The first standard Learjet rack constitutes the flow metering rack. It primarily consists of the gas and liquid flow loop plumbing components and the thermocouple amplifier electronics. Flow rate setting devices are mounted to this rack. These devices are pressure regulators and metering valves. Likewise, flow rate measurement devices such as pressure transducers and turbine flow meters are part of this rack assembly. There is also space for a gas supply cylinder (K-bottle), although in our experiments, gas was supplied from two compressed air cylinders, external to the test loop assembly and

secured aboard the aircraft within an aluminum housing. Dimension-wise, this rack is wide by 120 cm long by 120 cm high.

The second standard Learjet rack is designated as the data acquisition rack. This rack consists of the test section assembly, the flow visualization system (with the exception of the high speed video system), the data acquisition and control systems as well as tri-axial accelerometers, to monitor acceleration levels during parabolic flight. In our experiments, the tri-axial accelerometers were mounted aboard the DC-9 and not directly on the second rack. This rack also features an operator interface panel which is composed of a liquid crystal display, various toggle switches and two thumbwheels used to select program options. The second rack is 60 cm wide, by 60 cm long by 120 cm high.

The third, or custom-designed rack is a flat plate on which the back pressure regulator, the recirculation pump, the liquid supply tank and the two-phase collector / separator tank are fixed. This rack is mounted between the two standard racks. The complete flow loop assembly, which consists of these three racks occupies a total space of .61m by 1.83m and is fixed to Unistrut channels which are attached to mounting points within the aircraft. These fixtures allow for spacing adjustment between racks since the 51 cm

distances between hole patterns in the aircraft are set by design. In order to distribute flow loop assembly weight and thereby minimize damage to the fire-proof floor padding, plywood segments are introduced between the aircraft floor and the Unistrut channel mounts.

The flow loop system is composed of four distinct sections, namely the gas system, the liquid system, the two-phase flow test section assembly and the liquid recirculation system. A generic schematic of the flow loop system is presented in figure 4. Only important components of this flow loop are displayed in this schematic diagram.

The main purpose of this system is to provide metered quantities of water and air to the test section assembly and consequently to collect the liquid for recycle while venting the air which exits the test section.

From the gas supply cylinder, there are two gas metering flow legs. Each leg consists of a pressure regulator, a pressure gauge, a solenoid valve and a square-edge orifice. For our experiments, the air flow rate was controlled by injecting air through one of two choked orifices, depending on the desired flow rate.

Each orifice has a different diameter, namely .691 mm and .183 mm. A turndown ratio of approximately 250 to 1 was obtained for the desired pressure range. The orifice plates are properly sized in such a manner as to achieve sonic velocity at the orifice for the desired range of flow rates. Superficial gas velocity, for flow through the small orifice can range from 0.05 to 2.0 m/sec., and through the large orifice from 2.0 to 25.0 m/sec. at atmospheric pressure conditions.

Thus, when air was injected through the small orifice, bubble and slug flow patterns were observed. Air injection through the large orifice is essential when the annular flow pattern is desired.

Temperature and pressure are measured upstream of each orifice and also in the common line after the orifice, since the gas metering flow legs merge into a tee once they clear the orifice area. If the absolute pressure measured upstream of the orifice, is at least two times greater than the pressure downstream of the orifice, the flow of gas through the orifice is choked.

Hence, once sonic velocity is achieved, the gas mass flow rate becomes a function solely of the upstream temperature and pressure. More accurately, as shown by Bean (1971), the gas mass flow rate is a direct function of the

orifice discharge coefficient, the sonic flow function of an ideal gas, the ratio of the real to ideal gas sonic flow functions, the inlet stagnation pressure and varies as the inverse square root of the inlet stagnation temperature.

Therefore, the mass flow rate of injected gas can be determined from the following mathematical expression:

$$\dot{m}_g = C\left[\frac{P_{1S}}{\sqrt{T_{1S}}}\right]\phi^*_i\left(\frac{\phi^*}{\phi^*_i}\right)$$

, where ϕ_I^* is the sonic flow function of an ideal gas, (ϕ^*/ϕ_I^*) is the ratio of the real to the ideal gas sonic flow functions, P_{1S} is the inlet stagnation pressure, T_{1S} is the inlet stagnation temperature, a is the throat area of the square edged orifice, C is the orifice discharge coefficient and $\dot{m}_g$ is the gas mass flow rate.

Furthermore, the sonic configuration eliminates the effect which changes in downstream pressure may have upon volumetric gas flow rate.

Since it is possible for the small orifice to be blocked, the gas flow rate is verified with a wet test meter before each flight. Prior to each experiment, the upstream pressure is set with a pressure regulator. During the experiment, the upstream pressure and temperature were recorded by the data acquisition computer via a pressure transducer and a copper-constantan (T-

type) thermocouple, respectively. This data was acquired at 1 Hz, subsequently making possible the calculation of gas mass flow rate and superficial velocity based on these measurements. The air flow system was calibrated from time to time, in order to ensure that accurate gas flow rates could be set and measured. Several experiments have shown that this air flow configuration provides a steady gas mass flow rate to the test section assembly. Typically, steady mass flow rates of air within 5 to 10 % of the desired set point are achieved in the present experiments. This observation has also been reported by Bousman (1995).

Once the gas flow enters the common leg (tee), it passes through a check valve and from there it is injected via a single stainless steel tube into the co-flow section of the test section assembly. The check valve prevents or minimizes the backflow of water into the gas supply system.

The liquid supply tank holds four liters of distilled water. This feed tank is equipped with an air pressure loaded piston, whose main function is to maintain a constant pressure within the feed tank during reduced gravity maneuvers and also to prevent air bubbles from being entrained into the water system. Air from the gas supply cylinder is introduced on top of the aforementioned piston which in turn travels down a shaft located in the center

of the feed tank. As a result, water exits from the bottom of the liquid supply tank and after flowing through a screen mesh which acts as a filter, it splits into two paths, namely the test flow and the purge flow.

In the present experiments, the test flow which represents the liquid flow rate was controlled by a pair of metering valves connected in parallel. For the purpose of flow setting reproducibility, these valves were manually adjusted with micrometer handles.

The liquid flow rate is a direct function of physical properties of distilled water, the settings of the metering valves and also the air pressure existent above the piston. After the liquid flow is metered with a turbine flow meter, it passes through an electrically-actuated solenoid valve, past a check valve and continues its path through a conductivity reference cell.

The turbine flow meter provides a digital readout of the water flow rate via the data acquisition system. From time to time, the liquid system was calibrated so as to provide a liquid flow rate which was within the desired experimental uncertainty range. Typically the water flow rate was within 5 to 10% of the desired set point, similar to the gas flow system. Both liquid and gas supply systems make use of solenoid activated on-off valves which allow the data

acquisition computer to respectively start and stop the flow whenever necessary during a flight trajectory. This feature is essential for test flow loop shut-off in case of emergency, such as uncontrollable leakage during periods of reduced gravity.

The conductivity reference test cell was not used in these experiments since void fraction measurements via capacitance probes were not taken. Likewise, the purge flow path, which is usually used to flush any gas bubbles trapped in the differential pressure measurement system, was not utilized since pressure drop data was not required for our investigation.

After the flow passed through the test section assembly, the resulting two-phase mixture entered the gas-liquid collector / separator tank. This tank is made out of aluminum and has a dual purpose of retaining the water and venting the air extracted from the two-phase mixture via a relief valve actuated by a pressure regulator.

Under reduced gravity conditions, buoyancy becomes relatively weak, thus in order to separate the continuous phase from the dispersed phase, the two-phase flow mixture is introduced through a series of concentric stainless steel screen mesh cylinders.

Due to the action of surface tension, water spreads across the screen mesh and remains attached to it during periods of reduced gravity. Consequently, during the 2-g pull-up of the DC-9 aircraft, this water drains off the screen mesh to the bottom of the collector / separator tank for recirculation purposes. This screen mesh is located around and between a circular plate in which large holes have been drilled to act as a water drain path to the lower chamber of the collector tank. While water is being drained, the separated air phase passes through the screen mesh and is subsequently vented via a relief valve into the aircraft cabin. The vented air, unlike the continuous phase, is not recovered. From time to time, liquid droplets are entrained within the vented air, especially when the highest flow rates are used.

When normal gravity conditions are achieved, namely between flight trajectories, water is pumped back to the liquid supply tank via a recirculation line. A centrifugal pump is used to recirculate the liquid phase. Two solenoid valves are simultaneously opened in order to achieve water recirculation and venting of the separated gas phase.

An important requirement for safe and effective operation of an experimental package aboard the DC-9 Reduced Gravity Aircraft, is that all non-standard

fluid devices such as the test section assembly, the liquid supply tank and the separator / collector tank, have to be hydrostatically tested at 1.5 times the maximum working pressure differential. With respect to this pressure differential, its lower end is approximately 27.6 kPa, in case the aircraft loses cabin pressurization.

2.4 Flow Visualization and Data Acquisition

During the course of this investigation, direct observation of the two-phase flow phenomena is essential for determining bubble flow patterns. According to Bousman (1995), flow features such as bubbles or slugs can be less than 2 cm in diameter or length, and yet can move with velocities greater than 5 m/s in a reduced gravity environment. Thus, the human eye does not provide adequate resolution for capturing two-phase flow details. Furthermore, standard video equipment which records images at 30 frames per second is not adequate for detailed resolution of two-phase flow under either normal or reduced gravity conditions.

In light of these restrictions, a high-speed video system is used to visualize the ensuing flow patterns. For performing our experiments, we used a high-

speed S-VHS video camera which can record the flow pattern information at a rate of 250 full images/second.

The video camera is mounted on a tripod-based aluminum pole, which is fixed to the aircraft floor, while the video recording system is mounted within a specially designed aluminum housing located across the aircraft cabin from the flow loop assembly. The camera can be swiveled around the support pole, depending on whether flow patterns were observed for the co-flow test section or the cross-flow test section.

Illumination for the test section assembly is achieved by using two strobe lights mounted on a Unistrut bar directly above the test section on either side of it. These strobe lights provide an effective shutter speed of 10 microseconds and do not affect the image recording accuracy of the high speed video system. Strobe lighting also maximizes the "freezing" action of the video camera in order to offset the effects of lower resolution film.

Due to its size, it is quite difficult to mount the video camera inside the flow loop assembly. Therefore, the video camera is positioned as shown in figure 5. This flow visualization arrangement makes use of a mirror mounted in front

of the video camera on the same Unistrut bar as the strobe lights. This mirror is angled at 45^0 over the test section so as to provide a full view of it.

During flight, prior to each set of trajectories, a small television monitor is hooked up to the video camera, in order to check for alignment of the test section with respect to the orientation of the mirror.

As described previously, visualization of ensuing flow patterns is performed via an optical box filled with water in case of the co-flow system and a flat Plexiglas surface in case of the cross-flow system. A black film laminated sheet is positioned beneath each test section to improve the resolution of generated bubbles.

The data acquisition and control system is a card cage standard bus computer system. Its central processing unit is a 386 chip with 20 MHz capability and 4 MB of random access memory. Three distinct cards can be used for data acquisition. Each has a 12-bit resolution and can accept 32 channels of single ended input voltages. An operator panel, consisting of a display unit, two thumbwheels, an "ENTER" button, an emergency stop button and several toggle switches for inputting desired flow conditions, controls the acquisition of data.

Electrical power is supplied aboard the aircraft from a 110 V, 60 Hz source which powers the data acquisition and control system, the air and water flow solenoid valves and the recirculation pump. A 28 Vdc electrical source is used to power the turbine flow meter, the absolute pressure transducers, the strobe lights, the high-speed video system and the thermocouple system.

During the experiment, software written in C monitors several data channels and records the outputs. Data is recorded in appropriate units; from the turbine flow meter as gallons per minute, from the absolute pressure transducers as absolute pounds per square inch and from the thermocouples as degrees Fahrenheit.

In particular, data concerning the temperature and pressure upstream of the test section, as well as air and water flow rates is recorded. Furthermore, the data acquisition system also calculates and records gas and liquid flow rates as superficial gas and liquid velocities in meters per second. Uncertainty errors in these measurements are 5 % to 10 % of the desired setpoint for both water and air mass flow rates, up to 5 % for the temperature measurement and 7.5 % for the absolute pressure transducers.

2.5 Experimental Tasks and Test Procedure

For conducting experiments, at least two operators are required. A third operator is necessary in case one of the principal operators experiences motion sickness (which occurred on several occasions).

Several tasks are performed prior to and during the flight. After the two-phase flow loop apparatus is installed aboard the aircraft, all necessary electrical and plumbing connections are made between the three racks. First, the water feed line is connected from the liquid supply tank, located on the tank rack, to an appropriate fixture on the flow metering rack. Next, the purge supply line is connected to the purge solenoids on the data acquisition system rack, which in turn are connected to the two-phase flow entry region on the flow metering rack.

Following this step, the two-phase flow return line is connected from the test section exit flange, located on the data acquisition system rack, to the separator / collector tank. Next, the data acquisition cable bundle from the flow metering rack is connected to the data acquisition rack, while the power

and control cables are connected to the tank rack and the operator panel control cable is connected to the data acquisition rack.

Once, these important connections are made, the test section assembly is installed on an Unistrut bar which joins the flow metering rack to the data acquisition rack, via two flanges, located respectively on the two-phase flow entry section and the two-phase flow return line. Another Unistrut bar, on which the flow visualization mirror and the two strobe lights are mounted, is fixed above the test section assembly in between the two standard racks. Orientation of the mirror with respect to the test section is checked using a television monitor connected to the S-VHS video system. Next, the alignment of the test section assembly is checked and the gas supply hose is fixed to the air injection nozzle.

The liquid supply tank is flushed and than filled with filtered water (for removal of organic contamination). Since the small orifice is primarily used in these experiments, we must check the flow through this orifice using both a wet test meter and the data acquisition system. If measured mass flow rate values differ by more than five percent, the orifice the orifice is checked for blockage. In case the orifice is in fine condition, the flow loop is visually inspected for possible leaks.

Next, the gas supply cylinder is checked and the system is pressurized to 103.40 kPa. Following this step, the ambient pressure is measured with each absolute pressure transducer and then the local barometric pressure is entered into the computer. The control system software compares this measurement with the correct barometric pressure and consequently adjust the zero offsets.

The high-speed video system is connected to the data acquisition and control system, and is tested in unison with the two strobe lights. A fresh video cassette is inserted into the video recording system for every flight. Each video frame has a real time digital stamp on it, which makes it possible to distinguish between trajectories. Strobe lighting is used to maximize the freezing action of the video system, but does not interfere with the real time digital stamp.

To reiterate, during flight two operators are necessary for conducting experiments. One operator controls the data acquisition software and is stationed in front of the computer control rack. The other operator is stationed in front of the flow metering rack and is in charge of setting gas and liquid flow rates. A third operator may be required to closely check the liquid

recirculation line and make sure that the flow loop does not develop any leaks, which would cause the abrupt termination of the experiment.

The first operator configures the data acquisition system by setting the following parameters: gravity level, gas orifice size depending on gas flow rate, data acquisition rate, test section diameter, type of liquid used, length of camera recording and total experiment time. Meanwhile, the second operator sets the desired superficial gas velocity by adjusting the appropriate pressure regulator. Consequently, this operator sets the liquid supply tank pressure to 207 kPa and sets the liquid flow rate using micrometer handles located on the two liquid supply valves.

Next, the first operator calibrates all test loop instruments by inputting appropriate instructions into the control system. Once the aircraft enters the reduced gravity trajectory, this operator instructs the data acquisition software to commence the experiment. Both operators monitor the flow loop apparatus for leaks and note the position of any air bubbles within the liquid supply tank in the eventuality that these bubbles are ingested into the liquid feed system. If such a problem occurs, then the second operator would try to adjust the piston inside the liquid supply tank by controlling the appropriate pressure regulator.

In such cases, however, most of the visual data is distorted, since coalescence of ingested air bubbles and nozzle injected bubbles would result in an erroneous flow pattern. Data of this nature is not taken into consideration since its validity is highly questionable. In case of an emergency, such as an uncontrollable leak caused by a loose plumbing connection, the first operator can push a panic button located on top of the control panel. This action closes all solenoid valves and causes the flow to stop.

To perform this experimental test procedure, the operators are strapped down with adjustable Velcro bands inserted through metal ring mounts fixed to the aircraft floor. In case one of the principal operators is injured or otherwise indisposed, he or she is removed to the rear of the aircraft and the third operator takes over the necessary duties.

After completing a set of six reduced gravity trajectories, the aircraft turns back in order to commence a new set of parabolas within the same airspace. This turn period lasts for approximately ten minutes. During the turn, water is recirculated back to the liquid supply tank, from the separator / collector tank. Air injection nozzles are removed and changed, to account for a different

aspect ratio of nozzle to pipe diameter. Likewise, the air supply hose is removed and connected to either the co-flow or the cross-flow test section, depending on which was previously used.

After each flight, the data are checked to see whether any malfunction of the acquisition system has taken place during the experiment and also to check if the desired flow rates have been obtained. Consequently, this data, which are stored as integers, are converted to voltages and from voltages to engineering units. Software driven calculations are performed in order to translate air and water flow rate values to superficial gas and liquid velocities.

CHAPTER 3

EXPERIMENTAL RESULTS and DISCUSSION

3.1 Non-dimensional Parameters

In general, for a two-phase flow system in both normal and reduced gravity environments, under isothermal conditions , the bubble diameter D_B is dependent on fluid properties, flow geometry, flow conditions and the gravitational acceleration.

Mathematically, this functional relation can be expressed as:

$$D_B = f(\sigma, \mu_c, \mu_d \rho_c, \rho_d, D_P, D_N, U_{LS}, Q_d, g),$$

where σ is the surface tension of the continuous (liquid) phase; μ_c and ρ_c are respectively the dynamic (absolute) viscosity and the density of the liquid phase while μ_d and ρ_d and the dynamic viscosity and density of the dispersed (gas) phase; D_P is the two-phase flow conduit (pipe) diameter; D_N is the gas injection nozzle diameter, U_{LS} is the superficial liquid velocity, Q_d is the volumetric gas flow rate and g is the gravitational acceleration depending on the operational environment.

We note that counting D_B, there are 11 independent terms in function (f) and 3 independent dimensions, namely: [M]: mass, [L]: length and [t]: time. Consequently, by applying the Buckingham-Pi theorem, after some algebraic manipulation keeping the relevant physics in mind, we obtain eight [(11)-(3)] non-dimensional parameters, namely:

$$D_B^* = f^* (Re_P, We_P, Fr_P, D_N^*, Q_d^*, \mu^*, \rho^*)$$

where $D_B^* = D_B / D_P$; we use D_P as the reference length since it is the pipe diameter and hence a relevant physical dimension in the problem (for the bubbly flow regime);

$Q_d^* = Q_d / Q_c = [Q_d] / [U_{LS}(\pi/4)D_P^2]$, where Q_c is the volumetric liquid flow rate;

furthermore:

$D_N^* = D_N / D_P$: gas injection nozzle aspect ratio;

$Re_P = \rho_c U_{LS} D_P / \mu_c$: Reynolds number = (Inertia force / Viscous force)

$We_P = \rho_c U_{LS}^2 D_P / \sigma$: Weber number = (Inertia force / Surface Tension force)

$Fr_P = \rho_c U_{LS}^2 / (\rho_c - \rho_d) g D_P$: Froude number = (Inertia force / Buoyancy force);

$\rho^* = \rho_d / \rho_c$: density ratio and

$\mu^* = \mu_d / \mu_c$: dynamic viscosity ratio .

Since in our experiments we are using water as the continuous phase and air as the dispersed phase we can remove (μ^*) from the functional relation (f^*). Furthermore, in a microgravity environment, the Froude number approaches infinity and can be removed from (f^*) since the buoyancy force becomes negligible compared to other forces acting on the bubble. In parallel, under reduced gravity conditions (0.01g - 0.02g, where g is the terrestrial gravitational acceleration), the buoyancy force is still small compared to other forces acting on the bubble during its generation process (the Froude number getting up to 340 for the present set of experiments).

Consequently, in a reduced gravity environment, using a given liquid phase and a given gas phase for a two-phase flow system, under isothermal conditions, we obtain the following dimensionless functional relation for the process of bubble formation in a continuous liquid flow:

$$D_B^* = f^* (Re_P, We_P, D_N^*, Q_d^*, \rho^*) \quad .$$

It is important to understand that the non-dimensional parameters considered in the present problem are global parameters and they do not render the complete physical picture which describes the bubble generation phenomena. In order to obtain a more accurate understanding of the physics involved in bubble formation within a liquid flowing through a pipe, non-dimensional parameters should be obtained from local balance of detaching and attaching forces acting on the bubble at the time of detachment.

3.2 Experimental Parameters and Uncertainty Estimates

Experiments are conducted using both the co-flow configuration and the cross-flow geometry, for three different sets of pipe diameter, namely 1.27 cm, 1.9 cm and 2.54 cm, in an air-water system. Two different ratios of air injection nozzle diameter to pipe diameter (D_N^*) are used, namely 0.1 and 0.2.

Volumetric gas and liquid flow rates (Q_d and Q_c , respectively) are varied from 10 to 200 cc/s, depending on pipe diameter. The present experimental work considers non-dimensional parametric ranges based on pipe Reynolds number (Re_P), pipe Weber number (We_P) and pipe Froude number (Fr_P).

Thus, as parametric ranges we consider Re_P = 1600-8500, We_P = 2-75 and Fr_P = 2-340.

In order to ensure data repeatability, two dive trajectories are executed for each acquired data point. Sometimes, during the air injection nozzle change operation, eventhough great care was taken to arrange the experimental test section, the nozzle was not concentric within the co-flow conduit. In such cases, the forming bubble would impinge on the pipe inner wall and take longer to detach than under normal conditions. Since these data points are erroneous in nature, they are not considered in the present investigation. Furthermore, due to the difficulty of operating the test flow loop during periods of reduced gravity, certain data points have to be taken more than twice, fact which reduces the number of acquired data points.

Experimental bubble diameter is obtained from the flight experiment video by using THIN 2.0© and OPTIMAS 5.1© image acquisition and processing software packages. Since the detached bubble is not perfectly spherical for all flow conditions, the bubble diameter is obtained by taking a geometric average of the bubble's minor and major axis.

First, an image of the detached bubble is captured by the freezing action of the <*Display / Digitize*> feature incorporated within THIN 2.0©. Next, using a

feature displayed by OPTIMAS 5.1©, namely <*Measurement Explorer*>, the spatial calibration of bubble diameter is achieved with respect to a chosen reference length, usually the flow conduit (pipe) inner diameter.

The geometric averaged bubble diameter for each of the three consecutively detached bubbles in the vicinity of the gas-injection nozzle is first calculated. Bubble diameter reported in this investigation is the arithmetic average of these three values.

Experimental error in acquisition of bubble diameter is within ±5% of the mean diameter value. Uncertainty errors in measurement are ±5 to ±10% of the desired setpoint for both water and air mass flow rates, ±3 to ±5% of the desired setpoint for the temperature measurement and ±3 to ±7.5% of the desired setpoint for the absolute pressure measurement.

3.2 Co-Flow Configuration

Variation of bubble diameter (D_B) with respect to volumetric gas flow rate (Q_d) is displayed in figure 6. Data for three different Re_P values are shown, namely, Re_P = 1930, We_P = 2.0, Fr_P = 2.3; Re_P = 2870, We_P = 4.5, Fr_P = 5.1 and Re_P = 4700, We_P = 11.7, Fr_P = 13.5. This data is obtained by using the 2.54 cm I.D. pipe with an air injection nozzle diameter to pipe diameter ratio

(D_N^*) of 0.1, by varying the superficial liquid velocity (U_{LS}) from 7.6 cm/s to 11.3 cm/s and consequently to 18.5 cm/s.

In this plot, error bars are shown when presenting bubble diameter values. The experimental error considered in acquiring bubble size is ± 5 % of the mean bubble diameter value. In all plots which follow figure 6 we have to consider this experimental error.

There are two important trends which we observe in this plot.

First, we can clearly see that as the superficial liquid velocity is increased, the detached bubble decreases in size, for a constant volumetric gas flow rate. We note that across the three presented curves the surface tension force is held constant (fixed D_N). In order to properly estimate the liquid drag force we have to consider the relative velocity term, ($ds/dt - U_{LS}$), where ds/dt is the velocity of the bubble center and U_{LS} is the velocity of the liquid flowing through the pipe. We note that in this relative velocity term, the ds/dt term plays an attaching role while the U_{LS} term plays a detaching role in the process of bubble formation. For a given Q_d , the surface tension and the gas momentum forces are fixed, hence as the superficial liquid velocity increases, the bubble detaching effects increase, giving rise to a .smaller generated bubble. These bubble detaching effects are caused primarily by the liquid flow surrounding the bubble.

Furthermore, we note that bubble diameter increases with increasing volumetric gas flow rate (Q_d), holding superficial liquid velocity (U_{LS}) constant. This fact is substantiated by considering the important forces which preside over the bubble formation process. Along any one of the curves shown in this plot the surface tension force is constant since we are dealing with a given liquid and a given nozzle injection diameter. Subsequently, the gas momentum force which is a bubble detaching force increases with increasing Q_d , therefore one would expect the bubble to be smaller at detachment as the volumetric gas flow rate is increased. However, along with Q_d , the bubble center velocity ds/dt is also increasing. Recall that ds/dt has attaching effects upon the bubble therefore this plot indicates that the ds/dt effects overcome the detaching effects of the gas momentum force since the bubble does increase in size with respect to volumetric gas flow rate.

Figure 7 shows the variation of bubble diameter as a function of volumetric gas flow rate (Q_d) with respect to change in aspect ratio of gas injection nozzle diameter to flow conduit diameter (D_N^*) from 0.1 to 0.2. This data is obtained by using the 1.9 cm I.D. flow conduit at a constant U_{LS} of 18 cm/s and the 1.27 cm I.D. pipe at a constant superficial liquid velocity of 45 cm/s. Corresponding non-dimensional flow parameters are Re_P = 3420, We_P = 8.4,

Fr_P = 17.4 for the 1.9 cm pipe and Re_P = 5740, We_P = 35.6, Fr_P = 164.2 for the 1.27 cm pipe.

It is shown, that for a given pipe diameter, the bubble diameter increases with increasing nozzle diameter at a set value of superficial gas velocity. However, note that for the 1.9 cm pipe, the bubble diameter increases drastically by changing D_N^* from 0.1 to 0.2, while for the 1.27 cm pipe increases minimally with this change (if at all).

For the 1.9 cm pipe I.D. case as we increase the gas injection nozzle diameter we increase the magnitude of the surface tension force, while decreasing the value of the gas momentum force. Since the surface tension force acts to attach the bubble to the gas injection nozzle, the formed bubble increases in size for a constant Q_d (fixed momentum force). The Weber number based on pipe diameter (We_P) is on the order of 8.

On the other hand, for the 1.27 cm pipe I.D. case, we have a We_P on the order of 36, therefore we can deduce that as the surface tension effect decreases the D_N^* effect diminishes. However, since the bubble diameter stays nearly constant this signifies that the attaching and the detaching forces are closely balanced. This stresses the use of a modified $(We_P)_m$ based on

the (ds/dt - U_{LS}) relative velocity term. The value of $(We_P)_m$ in this case is smaller than the We_P value, showing that bubble attaching forces can not be neglected with respect to bubble detaching forces.

Figure 8 presents the variation of dimensional bubble diameter (D_B) with increasing superficial liquid velocity for a given value of volumetric gas flow rate. The data presented in this figure is taken by using the 1.9 cm test section at a set volumetric gas flow rate of 51 cc/s, the 2.54 cm test section at a set Q_d equal to 61 cc/s and the 1.27 cm test section at a set Q_d equal to 15 cc/s. For the 1.9 cm test section, the superficial liquid velocity is increased from 11 to 27 cm/s, for the 2.54 cm test section, U_{LS} is increased from 8 to 15 cm/s and for the 1.27 cm test section, the superficial liquid velocity is increased from 8 to 14 cm/s. All these tests are performed using a ratio of air injection nozzle diameter to pipe diameter equal to 0.1.

It is shown that bubble diameter decreases with increasing superficial liquid velocity, at fixed values of volumetric gas flow rate, pipe diameter and gas injection nozzle diameter, stressing the effectiveness of surrounding liquid velocity as a means of detaching a forming bubble under reduced and microgravity conditions. Along any one of the three curves presented in this plot, the surface tension force and the gas momentum force are constant.

What changes is the bubble detaching effect caused by increasing superficial liquid velocity. Therefore, since the bubble is prone to detach as U_{LS} is increased, the bubble size decreases.

Note that the bubble diameter seems to decay quite slowly, if not, become asymptotic, with values of U_{LS} = 40 cm/s and higher. This could mean that ds/dt and U_{LS} are both increasing so that their respective attaching and detaching effects counterbalance each other.

In parallel, we note that the bubble diameter increases across the three curves from bottom to top (for a given U_{LS} value), fact which can be explained by the increasing Q_d effect. This change in bubble diameter is higher between the bottom curve and the center curve than between the center curve and the top curve, primarily because the I.9 cm pipe I.D. case and the 2.54 cm pipe I.D. case have similar volumetric gas flow rates (Q_d = 51 cc/s and 61 cc/s respectively) while the 1.27 cm pipe I.D. case displays a Q_d equal to 15 cc/s. As previously explained (figure 6), the bubble size is shown to increase with volumetric gas flow rate.

Additional data, which displays the important role played by flowing liquid and change of gas injection nozzle diameter on bubble detachment is shown in figure 9. Experimental data presented in this figure is obtained for a fixed pipe

diameter of 1.9 cm and a volumetric gas flow rate of 51 cm^3/s (cc/s). Two sets of gas injection nozzle diameter ratios, namely $D_N^* = 0.1$ and 0.2, are used.

We note the constraining effect which the flow conduit pipe wall has upon the detached bubble diameter at low superficial liquid velocity. For a given nozzle diameter and a given volumetric gas flow rate, both the surface tension force and the gas momentum force are fixed. However, at low superficial liquid velocity, the detaching effects of U_{LS} are diminished, hence the bubble can increase in size up to the value of the pipe diameter.

What is most interesting in this plot is that, independent of nozzle diameter, as the superficial liquid velocity becomes large (higher than 40 cm/s) the generated bubbles become comparable in size. It is noted that at such high values of superficial liquid velocity , the bubble detaching effects of U_{LS} must counterbalance the attaching effects of the surface tension force which increases with gas injection nozzle diameter.

A graph of bubble formation frequency (f_B) as a function of superficial gas velocity, is shown in figure 10. Data is presented for the 1.9 cm test section at $D_N^* = 0.1$, $U_{LS} = 18$ and 24 cm/s, as well as for the 1.27 cm test section at D_N^*

= 0.1 and U_{LS} = 45 cm/s. Note that for constant superficial liquid velocity, the bubble frequency of formation increases with increasing volumetric gas flow rate. As Q_d is increased, however, we note a steady decrement in the value at which the bubble frequency increases, eventually the trend appears to become asymptotic. The increasing trend of bubble formation frequency with volumetric gas flow rate can be explained by mass conservation. If we refer to the 1.27 cm pipe I.D. case we note that as shown in figure 7, the bubble stays more or less constant in size at such high superficial liquid velocities. From the expression $Q_d = f_B V_B$ we can see that if V_B , namely the bubble volume is constant, then with increasing volumetric gas flow rate the bubble formation frequency also increases.

Furthermore, at a fixed volumetric gas flow rate, the bubble formation frequency is shown to increase with increasing superficial liquid velocity. This again can be explained by mass conservation. With increasing U_{LS} , the bubble size decreases due to the detaching effect displayed by the superficial liquid velocity , hence the bubble formation frequency increases. In parallel, the time to detachment of a given bubble is decreasing with increasing superficial liquid velocity.

Bubble formation and subsequent detachment under reduced gravity conditions is experimentally observed to be an interesting phenomenon.

Unlike bubble generation under normal gravity conditions, which usually gives rise to relatively small sized bubbles due to the action of the buoyancy force , larger and more uniform spherical bubbles are obtained in the present reduced gravity experiments.

Figure 11 shows bubble generation at high surrounding liquid velocity under reduced gravity conditions (U_{LS} = 35 cm/s, Q_d = 20 cc/s, D_P = 1.27 cm, D_N^* = 0.2). It is observed that before detachment, the bubble becomes elongated forming an ellipsoid rather than assuming a spherical geometry. This departure from a spherical geometry can be attributed to the detaching effect of the surrounding liquid, which acts as a bubble detaching force and dominates over the surface tension force which tends to attach the bubble to the rim of the air injection nozzle.

Similarly, elongation of bubble before detachment also occurs at high volumetric gas flow rates, which gives rise to a detached bubble resembling a slug (U_{LS} = 16 cm/s, Q_d = 95 cc/s, D_P = 2.54 cm, D_N^* = 0.1). This fact is displayed in figure 12. The appearance of acorn-shaped slugs is worth noting in this photograph.

On the other hand, at low superficial gas and liquid velocities, the bubble assumes a somewhat spherical shape while forming, as depicted in figure 13 (U_{LS} = 11 cm/s, Q_d = 10 cc/s, D_P = 1.27 cm, D_N^* = 0.1). In this case, the forming bubble also displays a short neck length relative to the diameter of the air injection nozzle.

Figure 14 presents a graph of elongation length (En) as a function of volumetric gas flow rate (Q_d) with respect to superficial liquid velocity (U_{LS}). Data is presented for the 1.27 cm test section at Re_P = 2210, We_P = 5.3, Fr_P = 24.3; Re_P = 3937, We_P = 16.7, Fr_P = 77.2 and Re_P = 5740, We_P= 35.6 and Fr_P = 164.2; for a D_N^* = 0.1. By looking at the photographs presented in figures 11-13, we can see that it is quite intractable to properly define a bubble neck length. Instead we can define an elongation length given as En = $Y - .5D_B$, where Y is the distance from the gas injection nozzle tip to the center of the forming bubble and D_B is the detached bubble diameter.

It is observed that for low volumetric gas and liquid flow rates, the elongation length is small, being approximately equal to the air injection nozzle diameter. However, as the volumetric gas and liquid flow rates are increased, the elongation length also increases, resulting in an elongated neck region. At

these flow conditions, the elongation length deviates considerably from the value of the air injection nozzle diameter.

Furthermore, as the volumetric liquid flow rate is increased with respect to the volumetric gas flow rate, a bubbly jet regime develops. This phenomenon manifests itself by the appearance of bubbles which have a distorted spherical geometry and a greatly elongated neck region (greater than 3 times the gas injection nozzle diameter).

Variation of void fraction (ε) with the ratio of volumetric gas flow rate to volumetric liquid flow rate (Q_d/Q_c) for various flow conditions, is displayed in figure 15, for averaged values of ε. Void fraction is defined as the ratio of volume occupied by the gas phase to total volume of fluid within a given section of the two-phase flow conduit. Mathematically, this relationship can be written as [$\varepsilon = (2/3)D_B^3/D_P^2\Delta$], where Δ is the distance between the front of a detached bubble and the front of the previously detached bubble. Consequently, the maximum void fraction within any given section of the two-phase flow conduit, is $\varepsilon_{max.} = 2/3$, for the bubbly regime and $\varepsilon_{max.} = 1$, for the slug (Taylor bubble) regime. Therefore any value of the void fraction which exceeds 2/3, indicates formation of Taylor bubbles.

Data is presented at two different flow conditions, namely Re_P = 2318, We_P = 3.9, Fr_P = 8.0 and Re_P = 4579, We_P = 15.1, Fr_P = 31.2, for two different flow geometries, namely D_N^* = 0.1 and D_N^* = 0.2, for D_P = 1.9 cm. It is observed that the void fraction increases with increasing the volumetric gas flow ratio (Q_d/Q_c). It is also apparent that the given data scatter is more or less along a straight line, suggesting that the void fraction is not a function of the flow geometry, namely a function of pipe and nozzle diameters (D_P , D_N). Instead, the plot suggests that the void fraction is a function of solely the volumetric gas and liquid flow rates. If we consider the previously given mathematical relationship for the void fraction, we can write $\Delta = U_B t$, where U_B is the bubble velocity and t is the time in which this moving bubble covers the distance Δ. Along the same lines $D_B^3 = (Q_d t)/(\pi/6)$. If U_B is written as $(U_{GS}+U_{LS})$, since $Q_c = (\pi/4)D_P^2 U_{LS}$ and $Q_d = (\pi/4)D_P^2 U_{GS}$, we obtain a modified relationship for the void fraction, namely $\varepsilon = Q_d/(Q_c+Q_d)$. This states that indeed the void fraction is a sole function of the volumetric gas and liquid flow rates and is not in any shape or form related to the flow geometry, in other words the flow conduit pipe diameter and the gas injection nozzle diameter. On the other hand, in theory the experimental data should fall on a straight line with none if minimal scatter. A reason for why this does not occur may be the presence of a combination of experimental measurement error and error induced by compressibility effects.

Consequently, we note that the void fraction and hence the flow regime transition from bubbly to slug flow, can be controlled in a precise manner, using a single nozzle gas injection system by simply varying the volumetric liquid and gas flow rates. This manner of monitoring void fraction is therefore as effective as multiple nozzle injection along the periphery of the two-phase flow conduit, which however, lacks the ability to control coalescence of adjacent generated bubbles and hence uniformity of bubble size.

At a high volumetric gas flow rate relative to the volumetric liquid flow rate, a detached bubble and a forming bubble at the nozzle tip can merge, thereby giving rise to bubble coalescence at the air injection nozzle exit. From our reduced gravity experiments, it is observed that immediately after detachment, the rear end of the bubble deforms by flattening out, in this manner moving further away from the gas injection nozzle tip. Subsequently, the rear end of the detached bubble expands and the bubble resumes its quasi-spherical shape. During this expansion process, the rear end of the bubble moves towards the nozzle tip.

While the rear end of the detached bubble undergoes flattening and subsequent expansion, another bubble is formed at the nozzle tip. It is

experimentally observed that at relatively high gas flow rates the front of the forming bubble can catch up with the rear of the detached bubble , especially when the later is expanding. The merger of these two distinct bubble fronts results in coalescence and forms a larger size bubble. Furthermore, it is observed that a coalesced bubble can be smaller but close to the pipe diameter or can result in slug (Taylor bubble) formation.

For a fixed superficial liquid velocity, the onset of coalescence condition is characterized by a critical gas flux. In dimensionless form, the onset condition, can be described by a critical non-dimensional volumetric gas flow rate, $Q_{d\,critical}^{*}$ (where $Q_d^{*} = Q_d/Q_c$). This critical volumetric gas flow rate ratio depends on gas injection nozzle diameter, fact also shown for bubble generation under normal gravity conditions by Sada et al.(1978). In the present reduced gravity experiment, the value of $Q_{d\,critical}^{*}$ at which onset of coalescence occurs for $D_N^{*} = 0.1$ is observed to be 1.35.

3.3 Cross-Flow Configuration

Figure 16 presents a graph of bubble diameter (D_B) as a function of volumetric gas flow rate with respect to change in superficial liquid velocity.

Data is presented for three different flow conditions using $D_N^* = 0.1$ and the 1.27 cm test section, namely $Re_P = 2210$, $We_P = 5.3$, $Fr_P = 24.3$; $Re_P = 3937$, $We_P = 16.7$, $Fr_P = 77.2$ and $Re_P = 5740$, $We_P = 35.6$, $Fr_P = 164.2$. Data is obtained for three distinct values of superficial liquid velocity, namely U_{LS} = 17.4 cm/s, 31 cm/s and 45.2 cm/s.

Similar, to experimental data obtained for the co-flow configuration, we observe that the bubble diameter increases with increasing gas flow rate, for a constant superficial liquid velocity.

Once again, this fact is substantiated by considering the important forces which preside over the bubble formation process. Along any one of the curves shown in this plot the surface tension force is constant since we are dealing with a given liquid and a given nozzle injection diameter. Subsequently, the gas momentum force which is a bubble detaching force increases with increasing Q_d , therefore one would expect the bubble to be smaller at detachment as the volumetric gas flow rate is increased. However, along with Q_d , the bubble center velocity ds/dt is also increasing. Recall that ds/dt has attaching effects upon the bubble therefore this plot indicates that the ds/dt effects overcome the detaching effects of the gas momentum force since the bubble does increase in size with respect to volumetric gas flow rate.

It is interesting to note that for U_{LS} = 45.2 cm/s and U_{LS} = 31 cm/s, at low volumetric gas flow rates the generated bubbles are comparable in size to each other. However as the volumetric flow rate is increased these bubbles start to considerably differ in size. Again, this can be explained by the bubble attaching role played by ds/dt which overcomes and dominates the detaching role played by the gas momentum force as Q_d increases.

Moreover, at a constant gas flux, the bubble size decreases as the superficial liquid velocity is increased, the variation being as prominent as for the co-flow configuration. We note that as the superficial liquid velocity is increased, the detached bubble decreases in size, for a constant volumetric gas flow rate. Note that across the three presented curves the surface tension force is held constant (fixed D_N). We recall that in the (ds/dt - U_{LS}) relative velocity term, which we have previously discussed, the ds/dt term plays an attaching role while the U_{LS} term plays a detaching role in the process of bubble generation. For a given Q_d , the surface tension and the gas momentum forces are fixed, hence as the superficial liquid velocity increases, the bubble detaching effects increase, giving rise to a smaller generated bubble.

This observation further stresses the importance of liquid flow for detaching bubbles from a gas injection port within a flow conduit in a reduced gravity environment.

Next, the effect of air injection nozzle geometry on bubble diameter is presented in figure 17. In this figure, dimensional bubble diameter is plotted versus volumetric gas flow rate at two flow conditions, namely Re_P = 3937, We_P = 16.7, Fr_P = 77.2 (U_{LS} = 31 cm/s) and Re_P = 5740, We_P = 35.6, Fr_P = 164.2 (U_{LS} = 45.2 cm/s), for two different gas injection geometries, namely D_N^* = 0.1 and D_N^* = 0.2, using the 1.27 cm test section.

As we increase the gas injection nozzle diameter we increase the magnitude of the surface tension force. Since this force acts to attach the bubble to the gas injection nozzle, the formed bubble increases in size for a constant Q_d (fixed momentum force).

It is observed that at high superficial liquid velocity, bubble diameter tends to increase considerably with increasing the ratio of air injection nozzle diameter to pipe diameter. This fact differs from the observation made for the co-flow configuration, where at high superficial liquid velocities, the bubble diameter is similar in size, independent of gas injection nozzle aspect ratio (D_N^*). Thus, contrary to the observation made for the co-flow configuration, we may deduce that the bubble attaching and detaching forces do not

counterbalance each other, instead the attaching forces dominate the detaching forces as the volumetric gas flow rate is increased.

Along the same lines, variation of bubble diameter with respect to superficial liquid velocity is shown in figure 18. This graph displays data taken by using the 1.27 cm test section with a $D_N^* = 0.2$ at a constant $Q_d = 44$ cc/s, the 1.9 cm test section with a $D_N^* = 0.1$ at a constant $Q_d = 28$ cc/s and the 2.54 cm test section with a $D_N^* = 0.1$ at a constant $Q_d = 61$ cc/s.

It is observed that the bubble diameter decreases with increasing superficial liquid velocity for a given gas injection geometry, at a constant gas flow rate. The trend is similar to that displayed by the co-flow configuration, in that by increasing U_{LS} we increase the detaching forces acting on the forming bubble, hence the bubble decreases in size. Furthermore, we note that with increasing volumetric gas flow rate, the bubble increases in size, a fact also observed for the co-flow configuration. In addition, observe that the bubble diameter seems to decay quite slowly, if not, become asymptotic, with values of $U_{LS} = 40$ cm/s and higher. This could mean that ds/dt and U_{LS} are both increasing so that their respective attaching and .detaching effects counterbalance each other (a similar observation to the co-flow configuration).

Additional data displaying bubble diameter as a function of superficial liquid velocity and gas injection nozzle diameter is shown in figure 19. This plot features data taken with the 1.27 cm test section at a constant gas flow rate of 44 cc/s. For two different nozzle diameters (D_N^* = 0.1 and 0.2), the superficial liquid velocity (U_{LS}) is varied from 10 to 60 cm/s.

The trends observed in this plot are similar to those displayed by the co-flow configuration.

Once again, we note the constraining effect which the flow conduit pipe wall has upon the formed bubble diameter at low superficial liquid velocity. For a given nozzle diameter and a given volumetric gas flow rate, both the surface tension force and the gas momentum force are fixed. However, at low superficial liquid velocity, the detaching effects of U_{LS} are diminished, hence the bubble can increase in size up to the value of the pipe diameter.

Furthermore, we observe that independent of nozzle diameter, as the superficial liquid velocity becomes large (higher than 40 cm/s) the generated bubbles become comparable in size. It is noted that at such high values of superficial liquid velocity, the bubble detaching effects of U_{LS} counterbalance the attaching effects of surface tension which increases with gas injection nozzle diameter.

Variation of bubble formation frequency (f_B) with respect to volumetric gas flow rate is displayed in figure 20. Data is presented for the 1.9 cm test section, D_N^* =0.1 at two values of superficial liquid velocity, namely U_{LS} = 18 and 24 cm/s; as well as for the 1.27 cm test section, D_N^* = 0.1 at a set U_{LS} = 32 cm/s. It is observed that the bubble frequency of formation increases as Q_d is increased at a constant value of the superficial liquid velocity.

Furthermore, at a fixed volumetric gas flow rate, the bubble formation frequency is shown to increase with increasing superficial liquid velocity. This again can be explained by mass conservation. With increasing U_{LS} , the bubble size decreases due to the detaching effect displayed by the superficial liquid velocity , hence the bubble formation frequency increases. In parallel, the time to detachment of a given bubble is decreasing with increasing superficial liquid velocity. This observation once again stresses the importance of surrounding liquid flow for providing the physical mechanism necessary to detach the forming bubble, independent of flow configuration. It is worth mentioning at this pont in time, that as observed from this plot, bubble formation frequencies are smaller in value for the cross-flow configuration than for the co-flow configuration at similar flow geometry (fixed D_P , D_N) and conditions (fixed Q_d and U_{LS}). This can be explained by the fact

that at similar flow geometry and conditions, bubbles generated using a co-flow configuration are smaller in size than bubbles formed using a cross-flow configuration.

A graph of void fraction (ε) averaged data as a function of volumetric gas flow rate with respect to volumetric liquid flow rate, is presented in figure 21. This experimental data is obtained at the following flow conditions: Re_P = 3420, We_P = 8.4, Fr_P = 17.4 (Q_c = 51 cc/s) and Re_P = 4579, We_P = 15.1, Fr_P = 31.2 (Q_c = 68 cc/s), using D_N^* = 0.1 and 0.2 for a constant pipe diameter of 1.9 cm.

In the cross-flow configuration, analogous to the co-flow geometry, it is observed that the void fraction increases with increasing the volumetric gas flow ratio (Q_d/Q_c). It is also apparent that the given data scatter is more or less along a straight line, suggesting that the void fraction is not a function of the flow geometry, namely a function of pipe and nozzle diameters (D_P , D_N). Instead, the plot suggests that the void fraction is a sole function of volumetric gas and liquid flow rates. Comparable to the void fraction values obtained for the co-flow configuration, the void fraction for the cross-flow configuration should be given as $\varepsilon = [Q_d /(Q_c+Q_d)]$. The fact that a data scatter exists and the void fraction values do not fall directly on this line

indicates the presence of some experimental error possibly coupled with compressibility effects.

For both the co-flow and the cross-flow configurations, void fraction is obtained by taking an average of ε values obtained at different times of a given flight trajectory, for two or three detached bubbles within a given section of the flow conduit, which could be visually inspected with the high speed video camera.

Comparison between values of bubble diameter obtained with the co-flow system and those obtained with the cross-flow system, is shown in figure 22. Data is presented for the 1.27 cm test section, $D_N^* = 0.1$ at $Re_P = 2210$, $We_P = 5.3$ and $Fr_P = 24.3$ ($U_{LS} = 17.4$ cm/s). We observe that at similar values of volumetric gas flow rate, superficial liquid velocity and air injection nozzle aspect ratio, bubbles generated by using the cross-flow geometry are slightly larger in size than bubbles obtained by using the co-flow configuration.

Further comparison between bubble diameters and void fraction values obtained by using the co-flow system with corresponding values obtained by using the cross-flow configuration is displayed in figure 23. The data presented in this plot, is obtained by using a I.9 cm diameter test section at a constant volumetric liquid flow rate of 68 cc/s with a 0.38 cm gas injection

nozzle diameter. The volumetric gas flow rate is varied from 21 to 70 cc/s. It is observed that at similar values of volumetric gas and liquid flow rates as well as similar gas injection nozzle and two-phase flow conduit diameters, bubbles generated by using the cross-flow configuration are slightly larger in size relative to those obtained in the co-flow geometry. Furthermore, in view of figure 22, this observation stresses the fact that in general, bubble sizes obtained with a co-flow system are smaller than those obtained with a cross-flow system, irrespective of flow geometry (fixed D_p,D_N) and/or flow conditions (fixed U_{LS},Q_d).

Moreover, we note, that the void fraction of the resulting two-phase flow obtained with the co-flow geometry is similar to that obtained using the cross-flow configuration. This closely follows the fact that the void fraction is independent of flow configuration. Recall, that from our previous discussion, we showed that the void fraction of the resulting two-phase flow is a sole function of volumetric gas and liquid flow rates and is therefore independent of flow geometry or flow configuration.

Coalescence of gas injection nozzle-detached bubbles is also observed for the cross-flow configuration, especially at high superficial gas velocity, hence

at high gas flow rates. The mechanism for coalescence is similar to that observed for the co-flow geometry, described in the previous section.

However, for the cross-flow geometry, an exact value for critical Q_d^* at which onset of coalescence occurs was not observed experimentally. Of interest is the fact that at $Q_d^* = 1.35$, the value at which bubble coalescence onset is observed for the co-flow system, generated bubbles are already merging and coalescing in the cross-flow system.

Furthermore, analogous to the co-flow configuration, at high volumetric gas and liquid flow rates, Taylor bubbles (slugs) are formed, as presented in figure 24 (U_{LS} = 25 cm/s, Q_d = 76 cc/s, D_P = 1.9 cm, D_N^* = 0.1). These bubbles display a highly elongated neck region and deviate from the spherical geometry, by assuming an ellipsoidal shape. At lower superficial gas and liquid velocities, generated bubbles decrease in size and display a shorter neck region, as shown in figure 25 (U_{LS} = 15 cm/s, Q_d = 32 cc/s, D_P =1.9 cm, D_N^* = 0.1). Strobe illumination, blurred these video images, as seen in these two pictures.

If the volumetric gas flow rate is greatly increased, so that Q_d^* ($=Q_d/Q_c$) is 2.85 or higher, air would jet out of the injection nozzle and impinge on the inner surface of the pipe wall directly opposite the nozzle. In this case, large

slugs, whose lengths exceed two to three times the pipe diameter are formed primarily by coalescence at the injector site.

The surface of these slugs is highly rippled. Furthermore, the overall motion of these slugs is wave-like and manifests itself in an apparently random fashion.

CHAPTER 4

THEORETICAL ANALYSIS

4.1 Theoretical Model

In order to better understand the physics of bubble generation under reduced gravity conditions we developed a model whose purpose is to augment experimental observations and shed some light on this rather complex phenomenon.

The present model is a modified version of work done by Kim (1992) and is also presented in Bhunia et al.(1997). Unlike Kim's work, this model incorporates the relative velocity term ($ds/dt - U_{LS}$) within the liquid inertia force term. This term is of utmost importance from a physical point of view since it describes bubble expansion relative to the surrounding liquid flow (ds/dt being the bubble center velocity with respect to the nozzle tip while U_{LS} is the superficial liquid velocity). By having made this omission, Kim shows several trends which do not match our current experimental data.

The theoretical model is based on a balance of forces acting on the bubble, which can be categorized into two groups, namely detaching or positive

forces and attaching or negative forces. As the name implies, detaching forces facilitate bubble detachment from the gas injection nozzle, while attaching forces inhibit this process from occurring. Following Newton's Second Law of Motion, the force balance equation may be written as :

$$F_B + F_M + F_\sigma + F_I + F_D = 0 \qquad (1)$$

The components of Equation (1) are:

$$\text{Buoyancy force} = F_B = (\rho_c - \rho_d) g V_B \qquad (2)$$

where ρ_c and ρ_d are the densities of the continuous phase (liquid) and the dispersed phase (gas) respectively, while V_B is the gas bubble volume. The term (g) represents the terrestrial gravitational acceleration. Eventhough the present investigation deals with a reduced gravity environment, the buoyancy force component is not dropped from the equation of motion. Its effects are minimal relative to the other forces but its presence is accounted for in this model.

Under reduced gravity conditions, acceleration due to gravity is 0.01g. For microgravity conditions (space-based) this gravitational acceleration reduces

further to 10^{-4}g. The present model considers a buoyancy force which acts vertically upwards and aids in the bubble detachment process.

Another detaching force which acts in the direction of gas injection is the gas momentum flux:

$$F_M = \rho_d \frac{Q_d^2}{\frac{\pi}{4} D_N^2} \qquad (3)$$

where Q_d is the gas volumetric flow rate and D_N is the gas injection nozzle diameter.

The surface tension force F_σ acts as an attaching force by pulling the bubble towards the injection nozzle along the nozzle rim and is written as:

$$F_\sigma = \sigma \pi D_N \qquad (4)$$

where σ is the liquid surface tension and D_n is the gas injection nozzle diameter. This formula takes into consideration the cylindrical nature of the bubble neck before detachment occurs (as seen from the high speed video snapshots presented in figures 11-13). Recall that we can write $\sigma(1/R_1+1/R_2)$

= (P_g-P_l), where P_g is the gas pressure inside the bubble, P_l is the pressure of the liquid outside the bubble, while R_1 and R_2 are radii of curvature. Since R_2 ,namely the radius of curvature representative of the cylindrical nature of the bubble neck is much greater in magnitude than R_1 which represents the gas injection nozzle radius, the term $(1/R_2)$ can be neglected with respect to the term $(1/R_1)$. Consequently, from a balance of surface tension and pressure forces in the viccinity of the nozzle tip where the bubble detaches, we obtain the previously given formula for F_σ .

Next, the inertia force F_I may be written as:

$$F_I = \frac{d}{dt}\left(\rho_d V_B \frac{ds}{dt}\right) + \frac{d}{dt}\left[\rho_c V_B C_{MC}\left(\frac{ds}{dt} - U_{LS}\right)\right] \qquad (5)$$

where C_{MC} is the added mass coefficient which varies depending on flow configuration and ds/dt is the bubble center velocity away from the origin located at the nozzle tip. The first term of equation (5) is called the bubble inertia and represents inertia force due to bubble motion. The second term of this equation is called liquid inertia and represents the inertia of the liquid which is pushed away from the injection nozzle by the accelerating surface of the expanding bubble. As we can see from the nature of this equation, the bubble inertia is an attaching force, while the liquid inertia force can be either

detaching or attaching depending on the relative magnitude of the superficial liquid velocity U_{LS} with respect to ds/dt, namely the bubble center velocity.

Last but not least of the forces acting on the bubble is the drag force F_D which is written as :

$$F_D = \tfrac{1}{2} S_D C_{DW} \rho_c U_{eff}^2 A_{eff} \qquad (6)$$

where C_{DW} is the drag coefficient with respect to the two-phase flow conduit wall, A_{eff} is the effective cross-sectional bubble area over which the drag force acts, S_D = +1 or -1 for U_{eff} smaller than or greater than zero respectively and U_{eff} is the relative velocity of a forming bubble with respect to the co-flowing liquid, written as $U_{eff} = (ds/dt) - U_{LS}$.

Similar to the inertia force, the drag force acting on the bubble can be either detaching or attaching, depending on the magnitude of the liquid superficial velocity U_{LS} relative to the bubble center velocity ds/dt.

In developing the present model, we consider the co-flow configuration displayed schematically in figure 26. In this diagram, a single circular nozzle of diameter D_N is located at the center of a circular pipe of diameter D_P. Through this pipe, flows a liquid of density ρ_c surface tension σ and dynamic

viscosity μ_c at a constant superficial liquid velocity U_{LS} and volumetric liquid flow rate Q_c (=.25$\pi U_{LS} D_P^2$). A gas of density ρ_d and dynamic viscosity μ_d is injected through the nozzle in the direction of liquid flow at a constant volumetric flow rate Q_d (=.25$\pi U_{GS} D_P^2$), where U_{GS} is the gas superficial velocity.

Furthermore, this theoretical model takes into account several assumptions. First and foremost among these assumptions is bubble sphericity throughout the formation process. Therefore, for the constant flow condition, the rate of change of bubble volume is given as :

$$Q_d = \frac{dV_B}{dt} = \frac{d}{dt}[\tfrac{\pi}{6} D_B^3(t)] = const. \qquad (7)$$

In addition to the spherical bubble assumption, the initial diameter of the bubble is taken as the nozzle diameter and the effect of the already detached bubble on the forming bubble is neglected from the theoretical analysis.

Kim (1992) developed an expression for the added mass coefficient used in the co-flow configuration, which is given as:

$$C_{MC} = \frac{1}{2} + 3\left(1 + \frac{1}{2\sqrt{2}}\right)\left(\frac{1}{\pi}\right)^{\frac{3}{2}} D_B^{*3}(t) \qquad (8)$$

where D_B^* is the dimensionless bubble diameter, non-dimensionalized as the ratio of bubble to pipe diameter. Likewise, for the co-flow geometry, Kim (1992) developed an expression for the drag coefficient C_{DW} taking into account the effect of the confining pipe wall. By following the experimental relation of Clift et. al. (1978), this term is written as:

$$C_{DW} = C_D \frac{1}{(1 - D_B^{*2})^3} \qquad (9)$$

In equation (9), C_D represents the drag coefficient of a bubble moving through an infinite expanse. For such an idealized case, there are several correlations for the drag coefficient of a spherical bubble, available in literature (Clift et. al., 1978). Along the same lines, literature on formulation of drag coefficient for a solid sphere moving through a quiescent infinite liquid is summarized by Bird et. al. (1960). Results computed by using the present theoretical model are compared with current experimental data. Consequently, we observe that by using the drag coefficient of a solid sphere, predicted bubble diameters are in better agreement with reduced gravity experimental results. In general, the drag coefficient of a bubble moving within a liquid is less than the drag coefficient of a solid sphere. This

is due to internal circulation of gas inside the bubble. The circulatory fluid motion inside the forming bubble which is induced by gas injection overwhelms this internal circulation. Therefore, the bubble behaves more like a solid sphere, with respect to the drag force. A similar observation was reported by Ramakrishnan et. al. (1969) and more recently by Kim et. al. (1994). In the present model we use the following drag coefficients, respective of given flow parametric ranges:

$$C_D = \frac{24}{\mathrm{Re}_B} \quad \text{for} \quad \mathrm{Re_B} < 2$$

$$C_D = \frac{18.5}{\mathrm{Re}_B^{0.6}} \quad \text{for} \quad 2 \le \mathrm{Re_B} \le 500$$

$$C_D = 0.44 \quad \text{for} \quad 500 \le \mathrm{Re_B} < 2000 \qquad (10)$$

In equation (10), $\mathrm{Re_B}$ represents the Reynolds number based on bubble diameter, which is expressed as $\mathrm{Re_B} = \rho_c U_{eff} D_B(t) / \mu_c$.

Recall that the relative velocity between the motion of the bubble center and the liquid flow, namely U_{eff} can be either negative or positive depending on the relative magnitudes of U_{LS} and ds/dt. When the bubble velocity is greater than the liquid velocity, the bubble front tends to push the liquid away from it and as a reaction experiences a drag force which inhibits bubble detachment. Likewise, if the liquid velocity is greater than the bubble center velocity,

surrounding liquid pulls the bubble front away from the gas injection nozzle tip and in this manner the role of liquid drag changes to that of a detaching force.

As a result of this drag force role duality, the bubble frontal area experiences these detaching or attaching force characteristics. Consequently, the effective area is:

$$A_{eff} = \frac{\pi}{4} D_B^2(t) \qquad \text{for} \quad U_{eff} > 0$$

$$A_{eff} = \frac{\pi}{4}(D_B^2(t) - D_N^2) \qquad \text{for} \quad U_{eff} < 0 \qquad (11)$$

Once a bubble has detached, it moves away from the gas injection nozzle, due to the surrounding liquid flow. While this motion is taking place a drift flow is initiated in the wake of the bubble, as discussed by Hahne and Grigull (1977). As a direct consequence of this drift flow, a suction effect is induced which acts as detaching force for the forming bubble. This force is however very small compared to the forces accounted for in this model, as shown by Zeng et. al. (1993) who also gives an estimate of this lift force. Thus, in our current investigation, the lift force created by the wake of the detached bubble is not considered.

In our present model, bubble formation takes place in two stages, namely the expansion stage and the detachment stage. During the expansion stage, the bubble grows radially as a result of gas injection via a single nozzle. The forming bubble remains attached to the gas injection nozzle rim. The end of the expansion stage is marked by the sum of detaching and attaching forces balancing each other, as shown in equation (1). During the expansion stage, $ds/dt = .5\, dD_B(t)/dt$ and $V_B = (\pi/6)D_B^3(t)$. With this in mind, the force balance equation at the end of the expansion stage is written as:

$$\frac{\pi}{6}(\rho_c - \rho_d)gD_B^3(t) + \rho_d \frac{Q_d^2}{\frac{\pi}{4}D_N^2} + \frac{1}{2}\rho_c C_{DW} S_D A_{eff}\left(\frac{1}{2}\frac{dD_B(t)}{dt} - U_{LS}\right)^2 = \pi D_N \sigma + \frac{d}{dt}\left[\frac{\pi}{6}\rho_d D_B^3 \frac{1}{2}\frac{dD_B(t)}{dt}\right] + \frac{d}{dt}\left[\frac{\pi}{6}\rho_c C_{MC} D_B^3(t)\left(\frac{1}{2}\frac{dD_B(t)}{dt} - U_{LS}\right)\right] \quad (12)$$

The bubble detachment phase commences once the expansion phase has ended. During the detachment stage, with additional gas injection the bubble continues to grow. Due to the surrounding liquid flow, the bubble moves away from the gas injection nozzle, however it develops a neck which also grows with time and keeps it attached to the nozzle. A portion of the gas injected during the detachment stage adds to the neck size while the remainder increases the bubble volume. The increase in neck size is negligible when compared to the increase in bubble volume during the detachment process.

Therefore, a further assumption is that the entire gas flow goes toward increasing the bubble size. As a result of this assumption, the bubble volume during the detachment stage is written as $V_B = (\pi/6)D_{Be}^3 + Q_d t$, where D_{Be} represents the bubble diameter at the end of the expansion stage. Furthermore, the bubble center, located at a distance Y from the nozzle tip, moves with a velocity ds/dt = dY/dt, faster than $.5dD_B(t)/dt$, which is the bubble center velocity during the expansion stage. Once again, by referring to equation (1) we can express bubble motion during the detachment stage as:

$$(\rho_c - \rho_d)g\left(\frac{\pi}{6}D_{Be}^3 + Q_d t\right) + \rho_d \frac{Q_d^2}{\frac{\pi}{4}D_N^2} + \frac{1}{2}\rho_c C_{DW} S_D A_{eff}\left(\frac{dY}{dt} - U_{LS}\right)^2 =$$
$$\pi D_N \sigma + \frac{d}{dt}\left[\rho_d\left(\frac{\pi}{6}D_{Be}^3 + Q_d t\right)\frac{dY}{dt}\right] + \frac{d}{dt}\left[\rho_c C_{MC}\left(\frac{\pi}{6}D_{Be}^3 + Q_d(t)\right)\left(\frac{dY}{dt} - U_{LS}\right)\right] \quad (13)$$

At the end of the detachment stage, the neck pinches off and the bubble detaches. The detachment criterion is discussed by Kim et al. (1994). Upon detachment it is assumed that the bubble neck collapses when the neck length becomes equal to the nozzle diameter, a condition which can be mathematically expressed as:

$$L_N = Y - \frac{1}{2}D_B \geq D_N \quad (14)$$

Next, the force balance equations, namely equation (12) and equation (13) as well as the detachment criterion, equation (14) are nondimensionalized with respect to a reference length $L_R = D_P$, a reference time $t_R = D_P/U_{LS}$ and a reference force $F_R = \rho_c U_{LS}^2 D_P^2$. As a result, equations (12), (13) and (14) can be rewritten as:

$$\frac{\pi}{6}\frac{D_B^{*3}}{Fr_P}+\frac{\pi}{4}\rho^*\left(\frac{U_{GS}^*}{D_N^*}\right)^2+\frac{1}{2}C_{DW}S_D A_{eff}^*\left(\frac{1}{4}\frac{U_{GS}^*}{D_B^{*2}}-1\right)= \\ \frac{\pi D_N^*}{We_P}-\frac{\pi}{8}U_{GS}^*(4C_{MC}-1)+\frac{\pi}{96}\frac{U_{GS}^{*2}}{D_B^{*2}}(8C_{MC}-3+2\rho^*) \qquad (15)$$

$$\frac{\pi}{6}\left(\frac{D_{Be}^{*3}+\frac{3}{2}U_{GS}^* t^*}{Fr_P}\right)+\frac{\pi}{4}\rho^*\left(\frac{U_{GS}^*}{D_N^*}\right)^2+\frac{1}{2}C_{DW}S_D A_{eff}^*\left(\frac{dY^*}{dt^*}-1\right)^2-\frac{\pi D_N^*}{We_P}= \\ \frac{\pi}{6}(\rho^*+C_{MC})\left(D_{Be}^{*3}+\frac{3}{2}U_{GS}^* t^*\right)\frac{d^2Y^*}{dt^{*2}}+\frac{\pi}{4}U_{GS}^*\left(2C_{MC}+\rho^*-\frac{1}{2}\right)\frac{dY^*}{dt^*}- \\ \frac{\pi}{4}\left(2C_{MC}-\frac{1}{2}\right)U_{GS}^* \qquad (16)$$

and the detachment criterion:

$$L_N^* = Y^* - \frac{1}{2}D_B^* \geq D_N^* \qquad (17)$$

In equations 15-17 we consider several non-dimensional parameters, namely: non-dimensional bubble diameter $D_B^* = D_B/D_P$; superficial gas velocity $U_{GS}^* = U_{GS}/U_{LS}$; non-dimensional nozzle diameter $D_N^* = D_N/D_P$; density ratio $\rho^* = \rho_d/\rho_c$ Weber Number $We_P = \rho_c U_{LS}^2 D_P/\sigma$; Froude Number $Fr_P = \rho_c U_{LS}^2/(\rho_c-\rho_d)gD_P$; non-dimensional bubble diameter at the end of expansion stage $D_{Be}^* = D_{Be}/D_P$; non-dimensional time $t^* = tU_{LS}/D_P$; dimensionless bubble center location $Y^* = Y/D_P$; Reynolds number $Re_P = \rho_c U_{LS} D_P/\mu_c$ and non-dimensional effective area $A_{eff}^* = .25\pi(D_B^{*2}-D_N^{*2})$ for $U_{eff}^*<0$ and $A_{eff}^* = .25\pi D_B^{*2}$ for $U_{eff}^*>0$. The drag coefficient C_{DW} is a function of Reynolds number based on bubble diameter Re_B, which in turn is a function of Re_P. Hence, the two Reynolds numbers can be related by the following mathematical expressions:

$$Re_B = \left|\frac{1}{4}\frac{U_{GS}^*}{D_B^{*2}} - 1\right| D_B^* Re_P \qquad \text{for the expansion stage}$$

$$Re_B = \left|\frac{dY^*}{dt^*} - 1\right| [D_{Be}^{*3} + \frac{3}{2}U_{GS}^* t] Re_P \qquad \text{for the detachment stage} \qquad (18)$$

As a result of equations (15) and (16), the non-dimensional bubble diameter at the point of detachment D_B^* can be expressed in functional form as:

$$D_B^* = f(\rho^*, D_N^*, U_{GS}^*, \mathrm{Re}_P, We_p, Fr_P) \qquad (19)$$

For given values of these functional arguments, the non-dimensional bubble diameter D_B^* is first computed at the end of the expansion stage and assigned the term D_{be}^*, by solving equation (15) using the Bisection method. This numerical method is preferred over the Regula Falsi method since it takes a fewer number of iterations to attain convergence to the same D_{be}^* value. With the obtained D_{be}^* value, equation (16), which is a second order non-linear ordinary differential equation, is solved using a fourth order Runge-Kutta method in order to determine the position of bubble center Y^* and the detached bubble diameter D_B^*. Next, the detachment criterion, namely equation (17) is checked using the computed values of D_B^* and Y^*. In case that the limiting condition of this equation, namely $L_N^* = D_N^*$ is not satisfied, a small time increment Δt^* is taken, all forces considered are recalculated and equation (16) is resolved to obtain new values for Y^* and D_B^*. As the detachment stage commences, we have the expression $Y^* = .5D_B^*$. However, with increase in time $[t^*+\Delta t^*]$, Y^* starts to increase faster than $.5D_B^*$ and the bubble neck length becomes equal to the gas injection nozzle diameter exactly at the instant when the bubble neck collapses and

detachment occurs. Therefore, the solution of equation (17) yields the detached bubble diameter.

Recall that in section 3.1 of Chapter 3, we discussed that a more appropriate term than U_{GS} (superficial liquid velocity) is Q_d (volumetric gas flow rate). Therefore, from now on, when we refer to U_{GS}^*, this term should be thought of as a function of Q_d, namely $U_{GS}^* = Q_d / (\pi/4)D_P^2 U_{LS}$.

4.2 Numerical Comparison with Experimental Results

Figure 27 presents a comparison of bubble diameter values, obtained from the present reduced gravity experiments, with numerical predictions obtained from the theoretical model. This graph shows variation of non-dimensional bubble diameter D_B^* with dimensionless superficial gas velocity U_{GS}^*. Two different aspect ratios of gas injection nozzle diameter to pipe diameter D_N^*, namely 0.1 and 0.2 along with two different corresponding Reynolds number Re_P for each D_N^* are presented for purpose of comparison. To generate this

plot we use ρ^{*} = 0.0012, Re_P = 1653, We_P = 1.97 and Fr_P = 4.1; Re_P = 4064, We_P = 8.9, and Fr_P = 10.3; Re_P = 2318, We_P = 3.9 and Fr_P = 8.0; Re_P = 4579, We_P = 15.1 and Fr_P = 31.2.

We note that as the superficial gas velocity is increased with respect to all other flow conditions and geometries being held constant, the detached bubble grows in size. Along the same lines, by increasing the ratio of nozzle injection diameter to pipe diameter, holding flow conditions constant, the bubble diameter increases, fact which is shown as valid by both theoretical and experimental data. Furthermore, numerical predictions are shown to be in good agreement with the experimental data.

Table 1 displays further comparison of theoretically predicted bubble diameter with present experimental results. A wide range of superficial liquid velocity, namely U_{LS} = 8.5 cm/s to 60.5 cm/s. is presented in this table. These values correspond to We_P = 1.9 to 63.4. It is shown that at high We_P, namely when inertia effects far outweigh surface tension effects (or better yet, when detaching forces considerably dominate attaching forces), there is considerable variation between experimental and numerical results.

At high superficial liquid velocity, hence at high We_P, the liquid inertia force is considerably higher than the surface tension force. Since it is the surface tension force which gives the forming bubble its sphericity, it is evident that at high values of We_P, the bubble shape starts varying to a great extent from the spherical geometry. This variation causes a change in the drag coefficient as well as the frontal area of the bubble. Therefore, at high We_P conditions, the presently employed theoretical model fails to accurately predict bubble size at detachment.

From visual observations of the flow field as well as the data presented in figure 27, it is concluded that under both reduced and microgravity conditions, the present theoretical model is valid up to a maximum We_P of 30. Another parameter closely coupled with the We_P is the pipe Reynolds number Re_P which also depends on the pipe diameter. For an air-water system which uses a 2.54 cm inner diameter pipe, We_P = 30 corresponds to a Re_P of approximately 7500.

Figure 28 presents a comparison of numerical and experimental non-dimensional bubble formation time (written as $t^* = U_{LS}t/D_P$) for various values of the ratio of superficial gas velocity to superficial liquid velocity, U_{GS}^*. Note that for both nozzle diameter aspect ratios, namely D_N^* = 0.1 and 0.2, at low

values of U_{GS}^{*}, bubble formation time decreases sharply with increasing U_{GS}^{*} until an asymptotic limit is reached. Beyond this limit the bubble formation time remains almost constant irrespective of U_{GS}^{*}, however as it is empirically observed this limit varies depending on test section diameter. Furthermore, it is observed that the bubble formation time increases as the nozzle diameter aspect ratio is increased, for all values of U_{GS}^{*}; hence the bubble takes a longer time to detach as the gas injection nozzle diameter is increased. For generating this plot, we use Re_P = 2667, We_P = 3.8 Fr_P = 4.4, with D_N^{*} = 0.1 and Re_P = 2318, We_P = 3.9, Fr_P = 8.0 with D_N^{*} = 0.2.

4.3 Range of Dimensionless Variables

As previously described, at high gas flow rates, a detached bubble and a forming bubble at the nozzle tip can merge, thereby resulting in coalescence of bubbles at the nozzle exit. In the present reduced gravity experiments, the critical U_{GS}^{*} for onset of coalescence to take place for D_N^{*} = 0.1 is observed to be 1.35 for the 1.27 cm test section which displays the co-flow configuration. Since the present investigation concentrates on single bubble generation,

numerical predictions of results under reduced and microgravity conditions which are discussed in the following chapter, display an upper limit of U_{GS}^{*} equal to 1.35.

In a reduced gravity environment, a single spherical bubble can grow to the size of the pipe diameter before it detaches ($D_B^{*} = 1$). In case the bubble does not detach at this point, it forms a Taylor bubble, namely a highly elliptical bubble whose length is greater than the inner diameter of the two-phase flow conduit. Theoretically, the model at hand can predict non-dimensional bubble diameter up to D_B^{*} equal to 1.

However, note that if the bubble diameter grows close to the pipe diameter before the bubble detaches, the surrounding liquid flow is blocked by the forming bubble. This bubble growth constricts the liquid flow area. The prevalent situation leads to high local liquid velocity and consequently high liquid inertia. In the ensuing competition between liquid inertia and surface tension, the former prevails thus causing the bubble to deviate from its otherwise spherical shape.

Consequently, the forming bubble assumes an elongated shape, by displaying an elongated neck region, as discussed in Chapter 3. The drag

coefficient and the frontal area of an elongated bubble are different from those of a spherical bubble as used in the present theoretical model. Since the current theoretical work does not take into account the variation in drag force due to bubble shape change, it can not be used for accurate prediction of detached bubble size as the bubble diameter approaches the pipe diameter in size ($D_B^* = 1$). Figure 27 shows that under reduced gravity conditions, numerical predictions obtained from the model at hand agree well with experimental D_B^* equal to 0.94. Hence, the cut-off D_B^* value is taken to be 0.95 for all numerical predictions.

CHAPTER 5

NUMERICAL PREDICTIONS FOR BUBBLE GENERATION UNDER REDUCED GRAVITY CONDITIONS

Since experimental data and numerical predictions are in good agreement, the present theoretical model is applied to predict bubble size, in particular bubble diameter, for bubble generation under reduced and microgravity conditions. Effects of gas injection geometry, flow conditions and fluid properties on the process of bubble formation are investigated.

Variation of bubble diameter D_B with respect to the superficial volumetric gas flow rate and the gas injection nozzle diameter D_N is presented in figure 29. In this figure, non-dimensional bubble diameter D_B^* is obtained as a function of dimensionless superficial gas velocity U_{GS}^* and non-dimensional gas injection nozzle diameter D_N^* by holding constant the dimensionless parameters $\rho^* = 0.0012$, $We_P = .91$, $Re_P = 1300$ and $Fr_P = 105.3$. The non-dimensional parameters used for generating this plot correspond to a co-flow system which uses air as the dispersed phase and water as the continuous phase. We note that D_B^* increases in a steady manner with the ratio of

superficial gas velocity to superficial liquid velocity, thereby indicating a direct proportionality between the bubble diameter and the gas flux.

All the detaching forces which act on the bubble, such as liquid drag, momentum flux and reduced buoyancy under reduced and microgravity conditions, increase with increasing gas injection flow rate. In parallel, the bubble inertia force which acts as an attaching force also increases, although at a much faster rate. Consequently, the bubble inertia force overweighs the effects of the aforementioned detaching forces, thereby increasing D_B^* with respect to U_{GS}^*.

Furthermore, figure 29 shows an increasing trend of bubble size with gas injection nozzle diameter, fact which can be explained by taking into consideration the detaching effect of gas momentum flux. From this figure it is evident that the effect of D_N^* is more prominent at high values of U_{GS}^*. At low values of U_{GS}^*, the gas momentum flux is not as significant as other forces which make up the force balance acting on the bubble at the point of detachment; whereas at high values of U_{GS}^*, the gas momentum flux plays a prominent role, hence a change in the gas injection nozzle diameter has a more significant impact on the overall force balance, thereby greatly influencing detached bubble diameter.

It is further observed that at $D_N^* = 0.1$, a Taylor bubble, in other words a slug, is not formed from a single bubble in the considered range of U_{GS}^*. However, as it is empirically observed, coalescence takes place for $U_{GS}^* \geq 1.35$ and the result of bubble coalescence can cause development of a slug. The plot shows that for $D_N^* = 0.2$ or higher, even before coalescence, a single bubble undergoes transition from bubbly to slug flow at a much lower superficial gas velocity. With increase in D_N^* from 0.2 to 0.3, transition from bubbly to slug flow takes place at a lower value of U_{GS}^*.

At this time it is important to note that all plots shown in figure 29 through figure 34, start at a value of U_{GS}^* equal to zero. When we produce the numerical results we start at a value of $U_{GS}^* = 0.001$, however in these plots due to the range of U_{GS}^* considered, this difference can not be visually observed. At a value of $U_{GS}^* = 0$, the non-dimensional bubble diameter presents a singularity, however at any other value of U_{GS}^* which exceeds zero, the bubble diameter has a finite value greater than zero. From a physical point of view, it is highly unlikely that a bubble will detach at very low values of U_{GS}^*. The present investigation shows good agreement between numerical and experimental results at a value of $U_{GS}^* \geq 0.3$. Therefore, beyond this U_{GS}^* value we can safely consider numerical predictions as valid.

Figure 30 presents the modified non-dimensional bubble diameter D_B^{**} as a function of non-dimensional superficial gas velocity, U_{GS}^{*} for various two-phase flow pipe diameters. In this plot, the bubble diameter is non-dimensionalized with respect to the gas injection nozzle diameter, $D_B^{**} = D_B / D_N$. In order to study the effect of change in pipe diameter D_P on detached bubble diameter D_B, the volumetric flux of liquid (Q_c) and gas (Q_d) are kept constant. For the same Q_c, an increment in D_P causes a reduction in the values of non-dimensional parameters, such as Reynolds number Re_P, Weber number We_P, Froude number, Fr_P and dimensionless nozzle diameter D_N^{*}.

It is observed that at a fixed U_{GS}^{*}, as the pipe diameter is increased, bubble diameter increases. We must stress that the observed trend in bubble diameter with respect to change in pipe diameter is the direct effect of change in superficial liquid velocity. Under constant Q_d and Q_c conditions, an increase in pipe diameter implies reduction of superficial liquid velocity U_{LS}. This fact leads to a reduction in the bubble detaching effect manifested by liquid drag and liquid inertia. Therefore, an increasing trend of bubble diameter with pipe diameter occurs. Furthermore, it is observed that over the entire range of U_{GS}^{*} the effect of change in pipe diameter upon detached bubble diameter remains similar.

The maximum value of U_{GS}^{*} used in figure 30 is 0.95. It is evident from this figure that at U_{GS}^{*} = .95, the modified non-dimensional bubble diameter approaches a value of 5, which corresponds to $D_B^{*} = D_B^{**} D_N^{*} = 1$. As previously indicated, the maximum value of D_B^{*} which can be predicted using the theoretical model at hand is 0.95. Therefore, to ensure that numerical predictions to not exceed the D_B^{*} =0.95 limit, the current computation is stopped at U_{GS}^{*} = 0.95. For generating figure 29 we use a fixed ρ^{*} = 0.0012, for the D_P curve - D_N^{*} = 0.2, Re_P = 1000, We_P = 1.1, Fr_P = 498; for the 1.5 D_P curve - D_N^{*} = 0.133, Re_P = 667, We_P = 0.32, Fr_P = 65.5; for the 2 D_P curve - D_N^{*} = 0.1, Re_P = 500, We_P = 0.136, Fr_P = 15.5.

The effects of superficial liquid velocity and gravity level *g* on bubble diameter D_B are displayed in figure 31. For a set of continuous and dispersed phase fluids (constant liquid and gas properties) at a constant gas flow rate and considering a fixed geometry (constant D_P and D_N), detached bubble diameter is computed for various values of superficial liquid velocity and g level conditions. As the superficial liquid velocity is increased, all the non-dimensional parameters such as Reynolds number Re_P, Weber number We_P, Froude number, Fr_P and the dimensionless superficial gas velocity U_{GS}^{*} change. However, the product of U_{GS}^{*} and Re_P ($Re_P U_{GS}^{*} = \rho_c U_{GS} D_P / \mu_c$) and

the ratio of We_P to Fr_P, defined as the Bond number ($Bo_P = We_P / Fr_P = (\rho_c - \rho_d)gD_P^2 / \sigma$) remain constant.

This figure shows variation of D_B^* with Re_P for various Bo_P values, which represent different g levels. It is evident that the bubble diameter shows a decreasing trend with increase in Re_P and hence increasing superficial liquid velocity, a phenomenon which is also experimentally observed. This is due to the fact that with increase in superficial liquid velocity, the detaching effect of liquid drag and liquid inertia increases, thereby leading to a reduction in detached bubble diameter.

It is further noted that under microgravity conditions, ($Bo_P = 0.0087$), there is a great deal of variation in D_B^* in the range of $Re_P = 500$ to $Re_P = 5000$. On the other hand, in a normal gravity environment ($Bo_P = 87$), bubble diameter decreases only by a small amount over the entire range of Re_P (500 to 5000). The Froude number based on pipe diameter ($Fr_P \approx U_{LS}^2/gD_P$) is in the range of .00016 to .016 for normal gravity (1g) and Fr_P = .16 to 16 for reduced gravity (0.01g). Under normal gravity conditions, the buoyancy force overwhelms the effect of liquid drag and liquid inertia (low Fr_P) which manifests itself through the superficial liquid velocity, U_{LS}. Thus an increase in superficial liquid velocity, does not have a significant reduction effect on

bubble diameter. On the other hand, under microgravity and reduced gravity conditions (high Fr_P), liquid drag and liquid inertia play a key role in the process of bubble detachment (via the U_{LS} term). Therefore, variation of the superficial liquid velocity affects the bubble diameter considerably.

The detaching effect displayed by the buoyancy force also explains the difference in bubble size obtained for different gravity environments as shown in figure 31. It is observed that at a fixed Re_P as the gravity level is reduced, by reducing the Bond number (and subsequently increasing the Froude number, Fr_P), larger bubbles are generated. However, it is of utmost interest to note that there is a saturation effect for the reduction of gravity level. The top curve plotted in figure 31 represents bubble diameter at the 10^{-4}g condition. Bubble size at the reduced gravity condition (10^{-2}g) is slightly less than that obtained at the microgravity condition, the difference being infinitesimal (visually negligible). This indicates that in a reduced gravity environment, the buoyancy effect upon bubble detachment is already significantly diminished. Therefore, any further reduction of the gravity level does not have a significant impact on the size of the generated bubble. For generating this figure, we use $\rho^* = 0.0012$, $D_N^* = 0.1$ and $Re_P U_{GS}^* = 500$.

Figure 32 presents the effect which Froude number Fr_P has on detached bubble diameter. In this figure non-dimensional bubble diameter D_B^* is plotted versus dimensionless superficial gas velocity U_{GS}^* for values of non-

dimensional parameters given as Re_P = 750, We_P = .608, ρ^* = .0012 and D_N^* = 0.1. The values of Froude number Fr_P considered are 2.8 and .028, corresponding to the reduced gravity condition and the normal gravity condition, respectively. It can be seen that for low superficial liquid velocity and low volumetric gas flow rate, the size of a bubble generated in a reduced gravity environment, is almost twice as large as that of a bubble formed in a normal gravity environment. This difference in bubble size with respect to gravity level reduces only slightly as the volumetric gas flow rate is increased.

In order to complete the present parametric study, variation of non-dimensional bubble diameter D_B^*, as a function of dimensionless superficial gas velocity U_{GS}^* , with respect to change in Weber number (We_P) is displayed in figure 33. It is observed that for the selected range of Weber number, the bubble diameter increases with increasing gas momentum flux. Figure 33 also shows the effect of the surface tension force on bubble size under conditions of reduced gravity and microgravity. Note that at a fixed value of the ratio of superficial gas velocity to superficial liquid velocity, as the surface tension force is increased by reducing Weber number, the bubble diameter increases. This observation stands to reason, since the surface tension force acts in order to attach the bubble to the gas injection nozzle.

The Weber numbers considered in this graph are .2, .5 and 1.0, while the other non-dimensional parameters considered are: $\rho^* = 0.0012$, $D_N^* = 0.1$, $Re_P = 600$ and $Fr_P = 22.4$.

Figure 34 presents the variation of bubble diameter with respect to change in surrounding liquid viscosity. In this figure, liquid viscosity is increased two fold, five fold and ten fold relative to a given value. All other non-dimensional parameters are held constant while the Reynolds number Re_P is reduced from 1000, to 500, to 200 and further to 100. It stands to reason that a more viscous fluid induces a higher liquid drag. For the considered range of Re_P, the superficial liquid velocity is always higher than the bubble center velocity (*ds/dt*). Therefore, the liquid drag acts as a detaching force. This fact explains the generation of smaller bubbles in a more viscous environment. It is further observed that the effect of liquid viscosity reduces with increasing U_{GS}^*. This fact indicates that the role of liquid drag in detaching the bubble is diminished with increasing gas momentum flux, which takes over the bubble detaching mechanism. For generating this plot, we use the following non-dimensional parameters: $\rho^* = .0012$, $Fr_p = 62.2$, $We_P = .54$ and $D_N^* = 0.1$.

CHAPTER 6

CONCLUSIONS

The present work which is the first study of its kind, is based on experimental data, obtained by performing experiments aboard the DC-9 Reduced Gravity Research Aircraft at the NASA Lewis Research Center. The experimental test section assembly makes possible the study of both co-flow and cross-flow configurations for single nozzle air injection within a water flow conduit.

It is experimentally shown, that for both co-flow and cross-flow systems, similar variational trends displayed by bubble generation via a single nozzle gas injector, do apply. Bubble diameter increases with increasing volumetric gas flow rate at constant superficial liquid velocity and flow geometry conditions. Along the same lines, bubble size decreases with increasing superficial liquid velocity, at constant volumetric gas flow rate and flow geometry conditions; thereby showing the important role which a continuous liquid flow plays in detaching a forming bubble in a reduced gravity environment.

Furthermore, it is observed that bubble diameter increases by increasing the ratio of air injection nozzle diameter to pipe diameter, for a given pipe diameter, at constant flow conditions.

Bubble frequency of formation varies directly with the superficial volumetric gas flow rate at constant superficial liquid velocity and flow geometry conditions. Likewise, the bubble formation frequency increases by increasing the superficial liquid velocity, with flow conditions and flow geometry kept constant; in this manner showing that the time to detachment of a forming bubble decreases as the liquid flow around the bubble is increased.

It is of interest to note that bubble size is smaller for the co-flow system than for the cross-flow configuration, at similar flow conditions and flow geometry. From experimental evidence, it is shown that void fraction can be readily controlled in case of single nozzle gas injection, by solely varying the volumetric gas and liquid flow rates.

Furthermore, it is experimentally observed that at a high ratio of volumetric gas to volumetric liquid flow rate (Q_d^*) coalescence of bubbles occurs at the exit of the air injection nozzle. The critical Q_d^* value for onset of coalescence

to occur is 1.35 for the 1.27 cm test section, at $D_N^* = 0.1$ for the co-flow configuration.

At low superficial liquid velocity and low volumetric gas flow rate, the detaching bubble takes on an almost spherical shape and displays a short neck region whose length is approximately equal to the diameter of the gas injection nozzle. On the other hand, at high superficial liquid velocity and high volmetric gas flow rate, this neck region becomes highly elongated, deviating in value from the gas injection nozzle diameter, while the detaching bubble assumes an ellipsoidal shape.

In order to explain and enhance the physical phenomena observed experimentally, a theoretical model is applied, which concentrates on single bubble generation in the dynamic and bubbly flow regime. This theoretical model is based on a force balance equation, which describes the overall bubble dynamics and is developed for the two stages of bubble generation, namely the expansion stage and the detachment stage. Two sets of forces, one aiding and the other inhibiting bubble detachment, thereby controlling bubble size, are identified.

The momentum gas flux aids, while bubble inertia and surface tension forces at the gas injection nozzle rim detract from bubble detachment. On the other hand, liquid drag and inertia have a dual role. In other words, these forces can act as detaching or attaching forces, fact which depends on the relative velocity of the bubble with respect to the surrounding liquid. The theoretical model predicts bubble diameter at detachment in good agreement with the performed reduced gravity experiments.

Effects of co-flowing liquid properties, flow conditions and gas injection nozzle aspect ratio on bubble size are investigated. It is observed that with reduction in gravity field, larger bubbles are formed. Reduction of gravity field below the reduced gravity environment (0.01g) has infinitesimal impact on bubble size. Therefore, bubbles generated in a microgravity environment are only slightly larger than those formed under reduced gravity conditions, the difference being barely noticeable. The theoretical model shows that bubble diameter decreases with increasing superficial liquid velocity, while bubble size increases with increasing pipe and nozzle diameter, keeping flow conditions and/or flow geometry constant. Furthermore, increasing liquid viscosity enhances the bubble detachment process, while surface tension plays an inhibiting role in bubble formation. Overall, the theoretical model displays similar variational trends for size of generated bubbles, when compared to

the experimental evidence. Numerical predictions agree well with experimental data, especially at low superficial gas and liquid velocities, when the forming bubble does not deviate greatly from the spherical shape.

In summary, this is the first study of its kind to experimentally investigate bubble generation via single nozzle gas injection within liquid flowing through a pipe, for both co-flow and cross-flow configurations under isothermal conditions of reduced gravity. Irrespective of flow configuration, bubble size is shown to decrease with increasing superficial liquid velocity (unlike bubble formation frequency), while detached bubble diameter increases with gas injection nozzle diameter and volumetric gas flow rate. In parallel, void fraction is shown to depend solely on volumetric gas and liquid flow rates and is independent of flow geometry and flow configuration. Furthermore, larger bubbles are obtained with the cross-flow system than with the co-flow system, although the difference in bubble size is not considerable (approximately 10% of the detached bubble diameter). It is of utmost importance to note that the present method of gas injection can prove more effective in producing uniform sized bubbles or slugs than its alternative, namely multiple port gas injection, for which coalescence between adjacent formed bubbles leads to non-uniformity in bubble size.

Results of the present work can be used in a wide range of space-based applications , such as thermal management and power generation, propulsion, cryogenic storage and long duration life support systems, necessary for programs such as NASA's Human Exploration and the Development of Space (HEDS).

REFERENCES

[1] Al-Hayes, R.A.M. and Winterton ,R.H.S., " Bubble Growth in Flowing Liquids", Int. J. of Heat and Mass Transfer, **24**, 213 (1981)

[2] Banerjee, S., "Space Applications", Mutiphase Flow and Heat Transfer: Bases and Applications Workshop, Santa Barbara, Calif., January (1989)

[3] Ostrach, S., "Industrial Processes Influenced by Gravity", NASA Reps. CR-182140, C-21066-G, NASA, Washington, DC (1988)

[4] Buyevich, Y.A. and Webbon, B.W., "Bubble Formation at a Submerged Orifice in Reduced Gravity", Chem. Engng. Sci., **51**, 21 (1996)

[5] Chuang, S.C. and Goldschmidt, V.W., "Bubble Formation due to a Submerged Capillary Tube in Quiescent and Co-flowing Systems", J. Basic Eng., **92** (1970)

[6] Clift, R., Grace, J.R., and Weber,M.E., "Bubbles, Drops and Particles", Academic Press, New York (1970)

[7] Colin, C., Fabre, J. and Duckler, A.E., "Gas-Liquid Flow at Microgravity Conditions-I, Dispersed Bubble and Slug Flow", Int. J. Multiphase Flow, **17**, 4 (1991)

[8] Colin, C., Fabre, J. and McQuillen, J.B., "Bubble and Slug Flow at Microgravity conditions: State of Knowledge and Open Questions", Chem. Eng. Comm., **141-142,** 4 (1996)

[9] Duckler, A.E., Fabre, J., McQuillen, J.B., and Vernon, R., "Gas-Liquid Flow at Microgravity Conditions: Flow Patterns and their Transitions", Int. J. of Multiphase Flow, **14**, 4 (1988)

[10] Hahne, E., and Grigull, U., "Heat Transfer in Boiling", Hemisphere (1977)

[11] Herold, K.E. and Kolos, K.R., "Bubbles aboard the Shuttle", Mechanical Engineering, **119**, 10, October (1997)

[12] Hill, T.J., "Gas-Liquid Flow Challenges in Oil and Gas Production", the 1997 ASME Fluids Engineering Division Summer Meeting, FEDSM97-3553 (1997)

[13] Jayawardena, S., Balakotaiah, V. and Witte, L. C., "Flow Pattern Transition Maps for Microgravity Two-Phase Flows", AICHE Journal, **43**, 6 (1997)

[14] Kawase, Y. and Ulbrecht, J. J., "Formation of Drops and Bubbles in Flowing Liquids in Terrestrial and Microgravity Environments", Ph.D. thesis, Case Western Reserve University, Cleveland, OH. (1992)

[15] Kim, I., "Modeling of Bubble and Drop Formation in Flowing Liquids in Terrestrial and Microgravity Environments", Ph.D thesis, Case Western Reserve Univ., Cleveland, OH (1992)

[16] Kim, I., Kamotani, Y. and Ostrach, S., "Modelling Bubble and Drop Formation in Flowing Liquids in Microgravity", AIChE J., **40**, 1 (1994)

[17] Klausner, J. F., Mei, R., Bernhard, D.M. and Zeng, L. Z., "Vapor Bubble Departure in Forced Convection Boiling", Int. J. Heat and Mass Transfer, **36**, (1993)

[18] Kumar, R., and Kuloor, N.R., "The Formation of Bubbles and Drops", Adv. Chem. Eng., **8** (1970)

[19] McCann, D. J. and Prince, R. G. H., "Regimes of Bubbling at a Submerged Orifice", Chem. Eng. Sci., **26** (1971)

[20] McQuillen, J. B. and Neumann, E.S., Learjet Two Phase Flow Apparatus", NASA Tech. Memo. 106814, NASA Lewis Research Center, Cleveland, OH (1995)

[21] Bird, R.B., Stewart, W.E. and Lightfoot, E.N., "Transport Phenomena", Wiley, New York (1960)

[22] Pamperin, O. and Rath, H., "Influence of Buoyancy on Bubble Formation at Submerged Orifices", Chem. Eng. Sci. **50**, 19 (1995)

[23] Rabiger, N. and Vogelpohl, A., "Bubble Formation and its Movement in Newtonian and Non-Newtonian Liquids", Encyclopedia of Fluid Mechanics, Vol. 3, Gulf Pub.. Houston (1986)

[24] Ramakrishnan, S., Kumar,R. and Kuloor, N.R., "Studies in Bubble Formation :I. Bubble Formation Under Constant Flow Conditions", Chem. Eng. Sci., **24** (1969)

[25] Sada, E., Yasunishi, A., Katoh, S. and Nishioka, M., "Bubble Formation in Flowing Liquids", Can. J. Chem. Eng., **56** (1978)

[26] Tsuge, H., "Hydrodynamics of Bubble Formation from Submerged Orifices", Encyclopedia of Fluid Mechanics, Vol. 3, Gulf Publications, Houston (1986)

[27] Van Krevelen, D. W., Hoftijzer, P. J, "Bubble Formation in Liquids", Chem. Eng. Prog., **46** 29 (1950)

[28] Wraith, A.E., "Two Stage Bubble Growth at a Submerged Plate Orifice", Chem. Eng. Sci., **26** (1971)

[29] Zeng, L. Z., Klausner, J. F. and Mei, R., "A Unified Model for the Prediction of Bubble Detachment Diameters in Boiling Systems: I. Pool Boiling", Int. J. Heat and Mass Transfer, 9 (1993)

[30] Bousman W. S., "Studies of Two-Phase Gas-Liquid Flow in Microgravity, NASA Contractor Report 195434 (1995)

[31] McQuillen, J. B., Neumann, E. S. and Shoemaker, J. M., "Two-Phase Flow Research Using the DC-9 / KC-135 Apparatus, NASA Technical Memorandum 107175 (1996)

[32] Mori, B. K., and Baines, W. D., "Studies of Bubble Growth and Departure from Artificial Nucleation Sites", ASME FEDSM '97 (1997)

[33] Bousman, W. S. and Dukler, A. E., "Studies of Gas-Liquid Flow in Microgravity, Void Fraction, Pressure Drop and Flow Patterns, Proceedings of the 1993 ASME Winter Meeting, Vol. 175 (1993)

[34] Bousman, W. S., McQuillen, J. B. and Witte, L. C., "Gas-Liquid Flow Patterns in Microgravity: Effects of Tube Diameter, Liquid Viscosity and Surface Tension, Int. J. of Multiphase Flow, Vol. 22, No. 6 (1996)

[35] Hewitt, G. F., "Multiphase Flow: The Gravity of the Situation", NASA Conference Publication 3330 (1996)

[36] Antar, B. N., "Gas-Liquid, Two-Phase Flow Diagnostics in Low Gravity", AIAA 96-2049, 27th AIAA Fluid Dynamics Conference (1996)

[37] Oguz, H. N., "Production of Gas Bubbles in Reduced Gravity Environments", NASA Conference Publication 3338 (1996)

[38] Bhunia, A., Pais, S. C., Kamotani, Y. and Kim, I. H., "Bubble Generation in a Co-flowing Liquid under Reduced Gravity Conditions", Canadian Society for Mechanical Engineering Forum, Toronto (1998)

[39] Bhunia, A., Pais, S. C., Kamotani, Y. and Kim, I. H., "Bubble Formation in a Liquid Co-flow Under Normal and Reduced Gravity Conditions", AIChE Journal, **44**, 7, (1998)

[40] Bean, Howard S., "Fluid Meters; Their Theory and Applications, ASME, 1971

Flow Conditions	U_{GS}^*	Computed D_B^*	Experimental D_B^*	% variation
U_{LS} = 8.5 cm/s, Re_P = 1615, We_P = 1.88, Fr_P = 3.88	.753 --- .965	.727 --- .762	.736 --- .815	1.22 --- .650
U_{LS} = 10.5 cm/s, Re_P = 2667, We_P = 3.84, Fr_P = 4.43	.336 --- .567	.572 --- .620	.530 --- .580	7.92 --- 6.90
U_{LS} = 18 cm/s, Re_P = 3420, We_P = 8.44, Fr_P = 17.40	.322 --- .822	.503 --- .663	.470 --- .670	7.02 --- 1.04
U_{LS} = 45 cm/s, Re_P = 5740, We_P = 35.57, Fr_P = 164.2	.260 --- .540	.432 --- .558	.510 --- .605	15.3 --- 7.77
U_{LS} = 60.5 cm/s, Re_P = 7684, We_P = 63.7, Fr_P = 294.20	.230 --- .320	.409 --- .459	.570 --- .610	28.25 --- 24.75

Table 1. Comparison of bubble diameter experimental values with numerical predictions of bubble size, $D_N^* = 0.1$

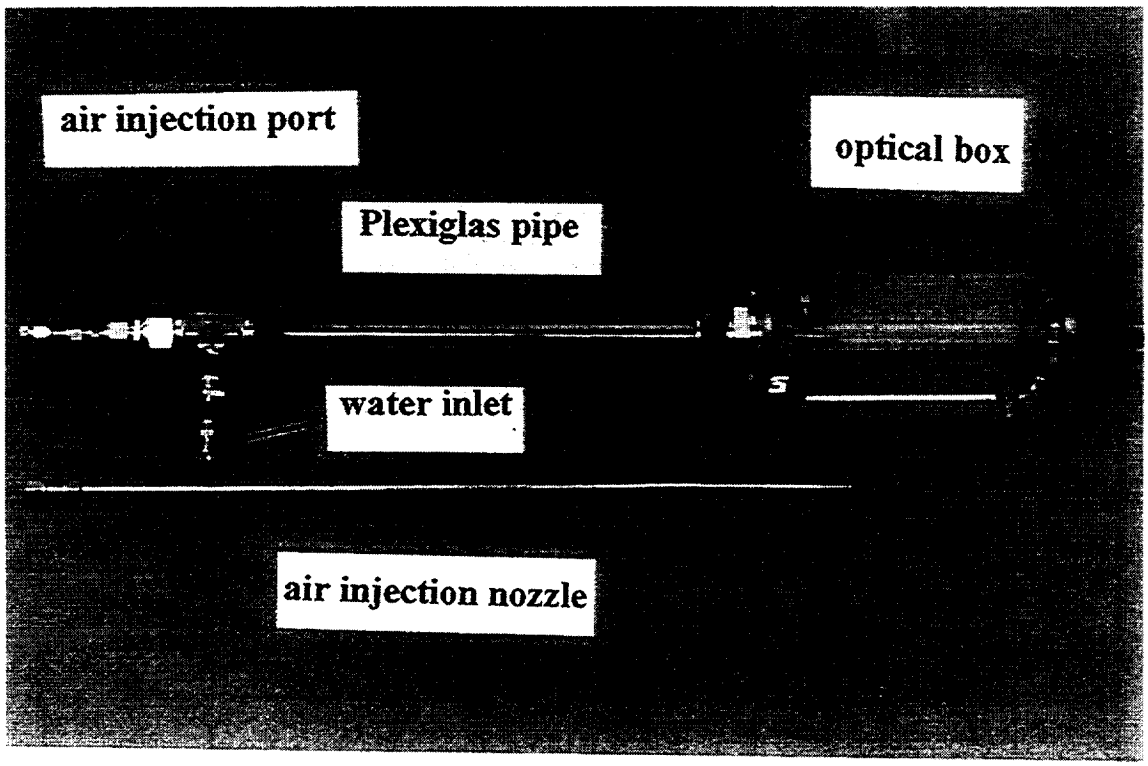

Figure 1. Experimental Co-flow System

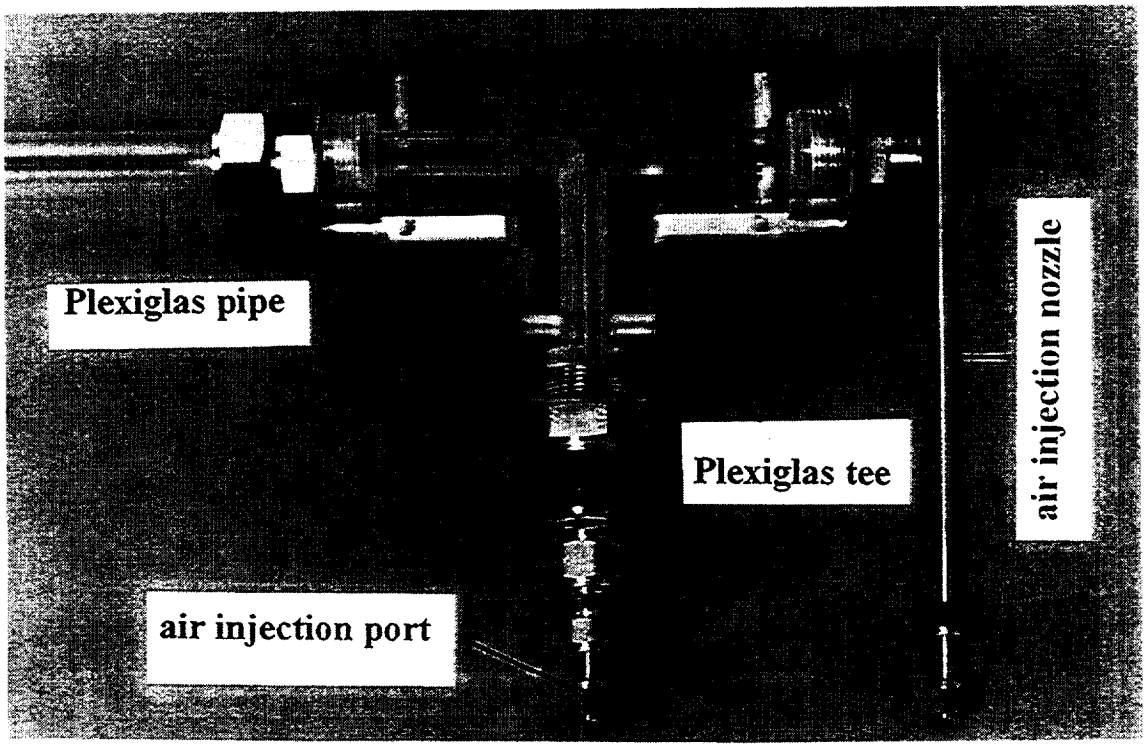

Figure 2. Experimental Cross-flow System

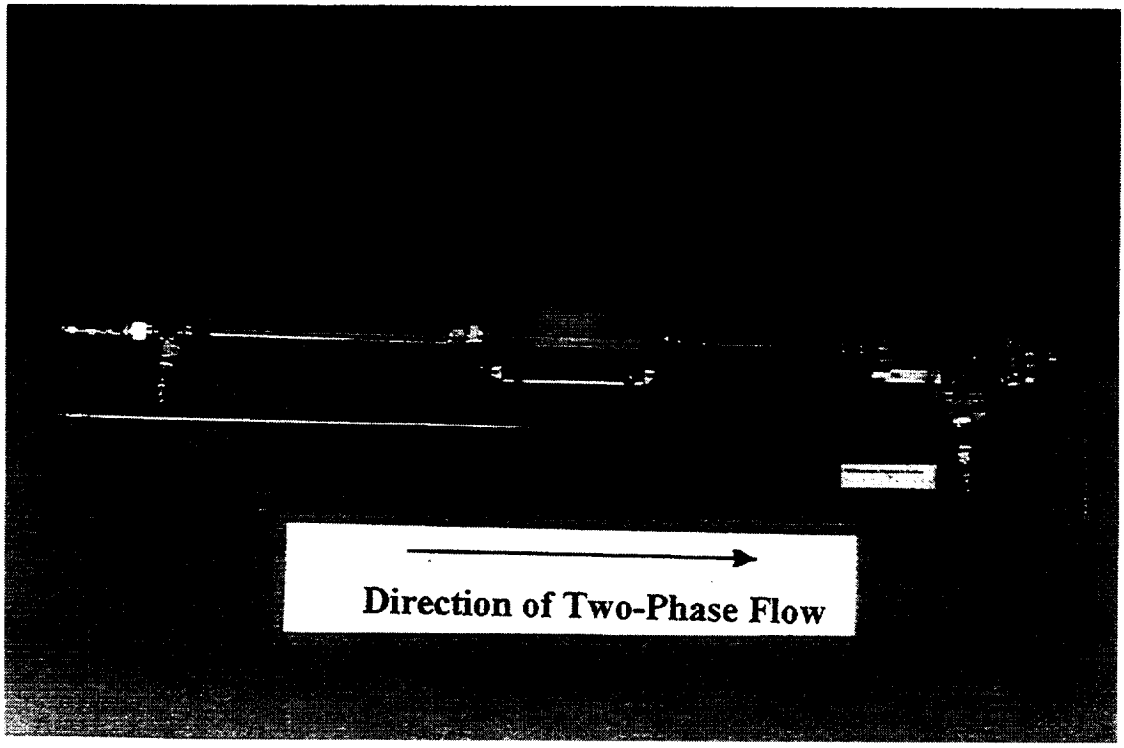

Figure 3. Experimental Test Section Assembly

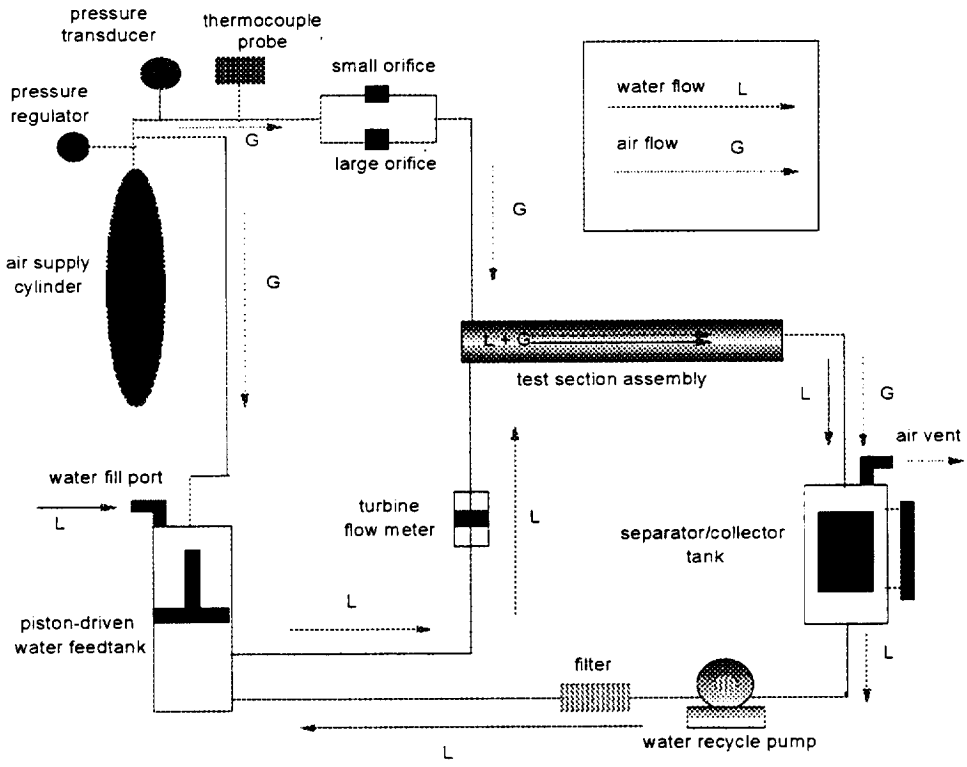

Figure 4. Test Flow Loop Layout

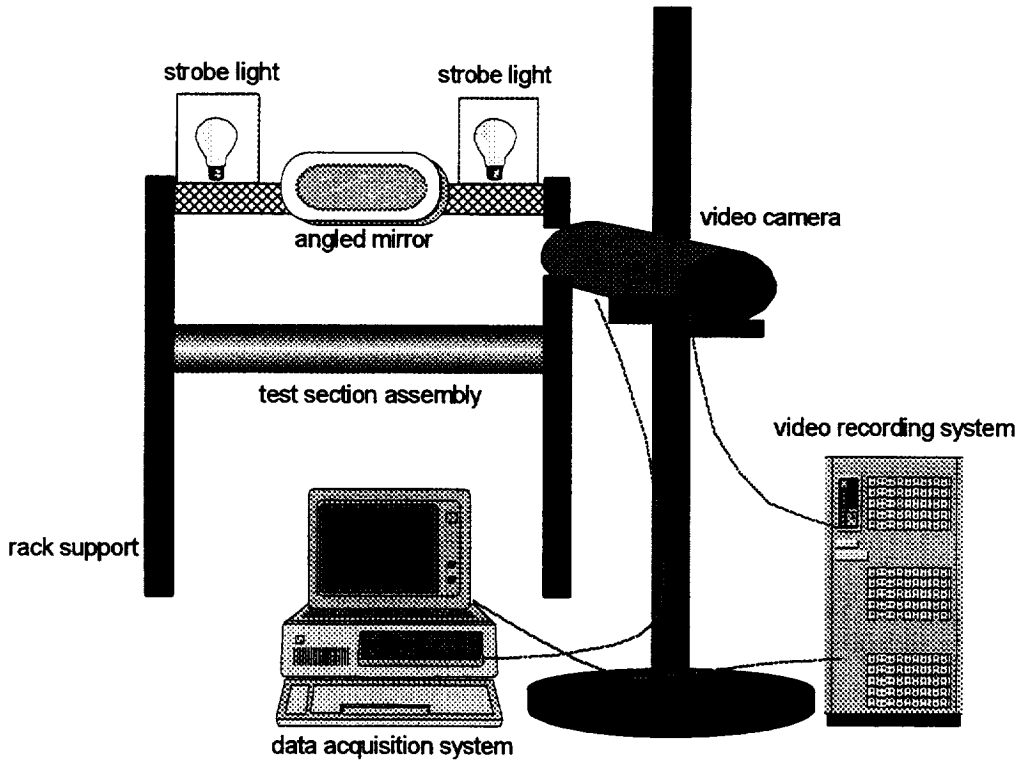

Figure 5. Flow Visualization Set-up

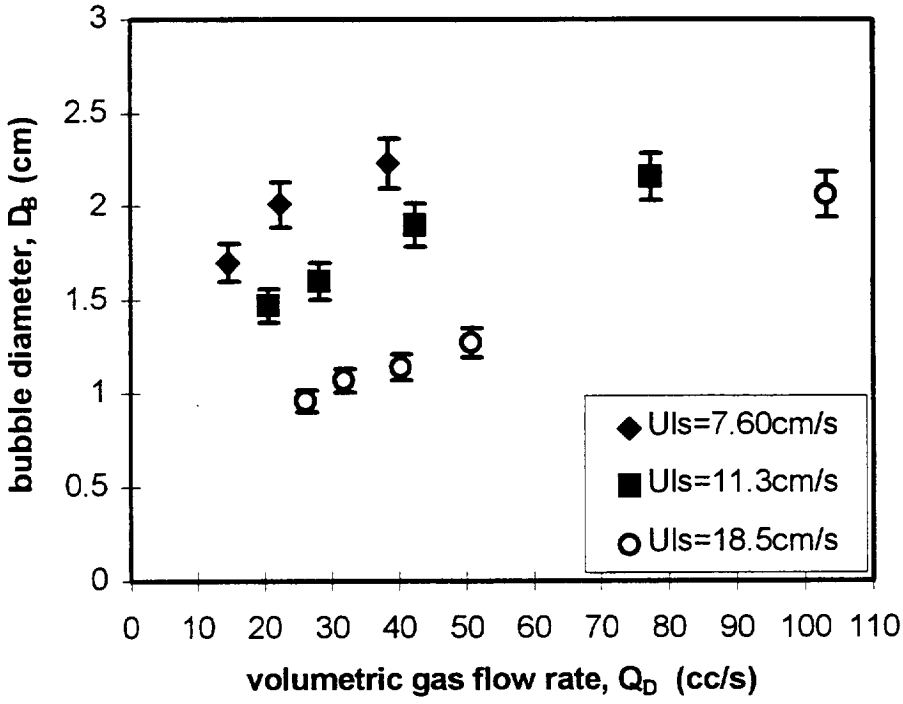

Figure 6. Co-flow configuration: Variation of bubble diameter D_B with volumetric gas flow rate Q_D , for D_P = 2.54 cm, D_N^* = 0.1; error bars are given as ± 5 % of the mean bubble diameter value

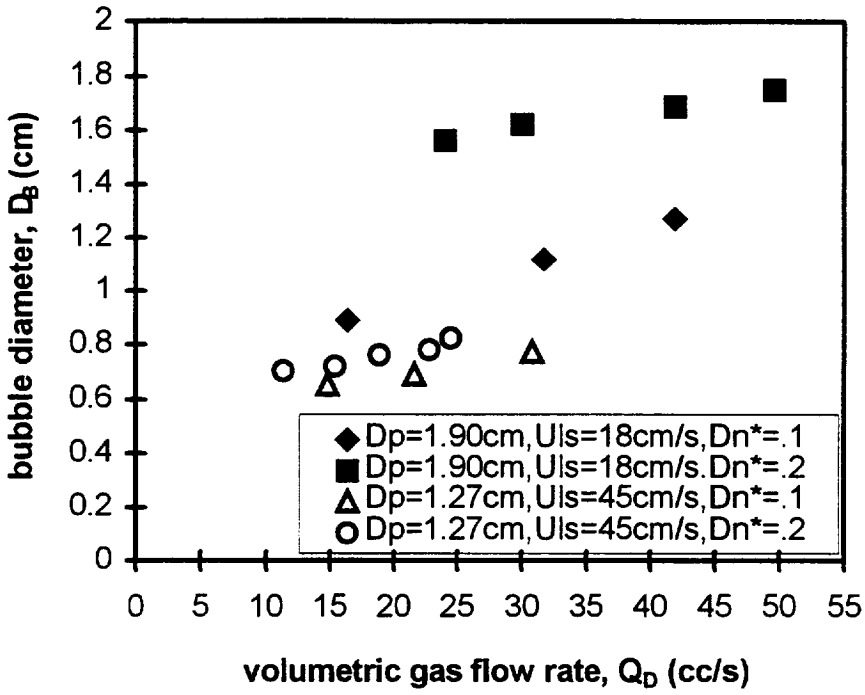

Figure 7. Co-flow configuration: Gas injection nozzle aspect ratio effect on bubble diameter D_B for the 1.27 and 1.9 cm test sections

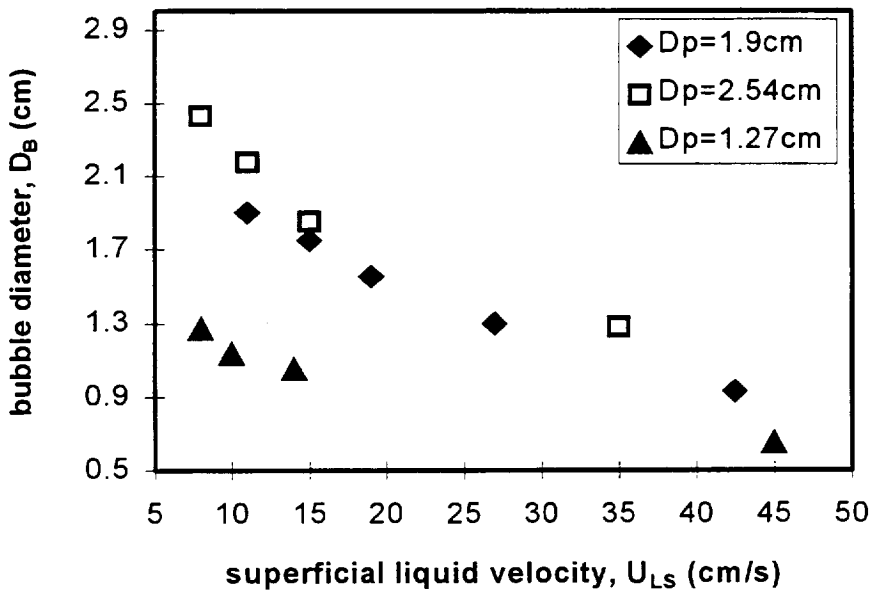

Figure 8. Co-flow configuration: Variation of bubble diameter with respect to superficial liquid velocity U_{LS} for D_P = 1.27 cm, Q_d = 15 cc/s; D_P = 1.9 cm, Q_d = 51 cc/s and D_P = 2.54 cm, Q_d = 61 cc/s; all test sections with D_N^* = 0.1

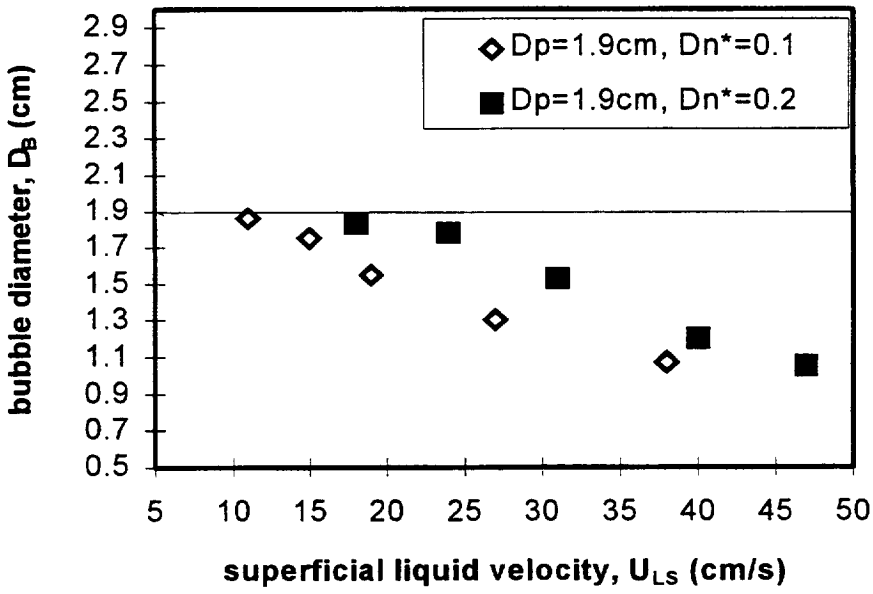

Figure 9. Co-flow configuration: Effect of gas injection nozzle diameter and superficial liquid velocity on bubble diameter. Fixed Q_d = 51 cc/s, D_P = 1.9 cm

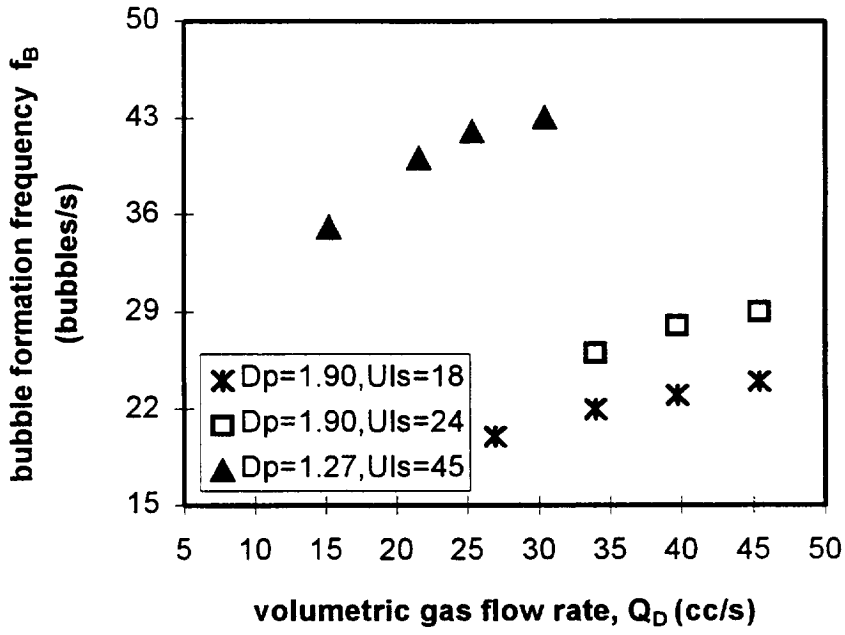

Figure 10. Co-flow configuration: Bubble formation frequency as a function of volumetric gas flow rate and superficial liquid velocity for the D_P = 1.27 and 1.9 cm test sections, D_N^*=0.1; (D_P values are in cm, U_{LS} values are in cm/s)

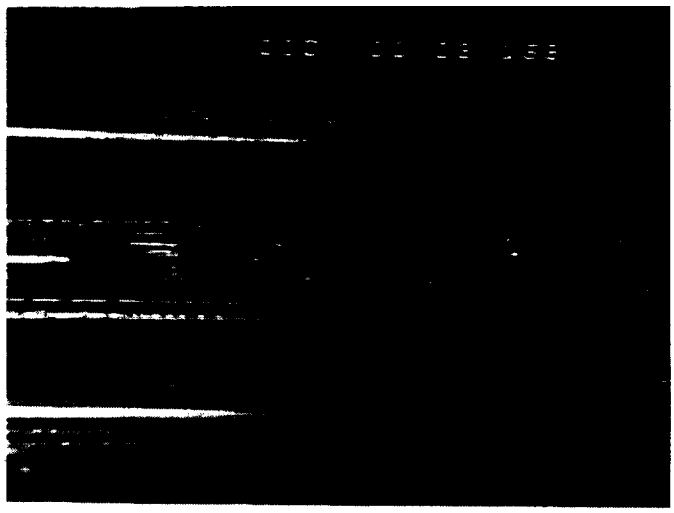

Figure 11. Co-flow configuration: Single video frame of bubble generation at high surrounding liquid velocity under reduced gravity conditions (U_{LS} = 35cm/s, Q_d = 20 cc/s, D_P = 1.27cm, D_N^* = 0.2)

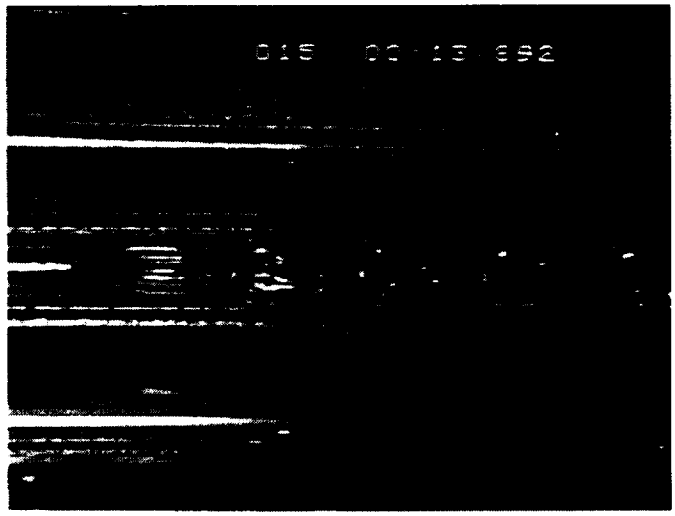

Figure 12. Co-flow configuration: Single video frame of bubble formation at high volumetric gas flow rate under reduced gravity conditions (U_{LS} = 16 cm/s, Q_d = 95 cc/s, D_P = 2.54 cm, D_N^* = 0.1)

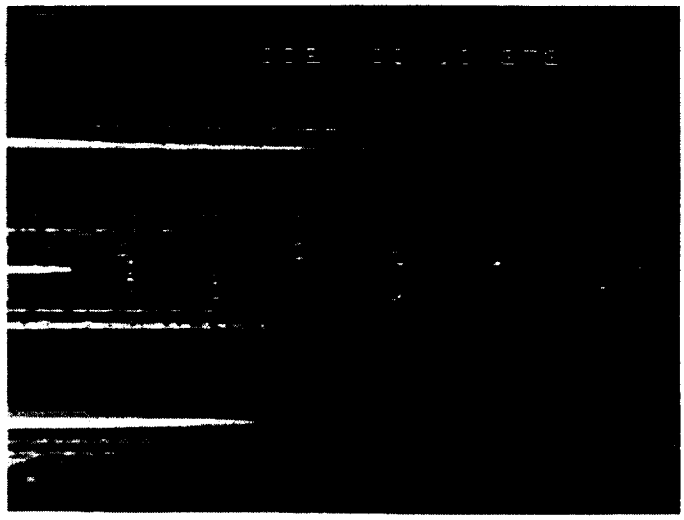

Figure 13. Co-flow configuration: Single video frame of bubble generation at low volumetric liquid and gas flow rates under reduced gravity conditions (U_{LS} = 11 cm/s, Q_d = 10 cc/s, D_P = 1.27cm, D_N^* = 0.1)

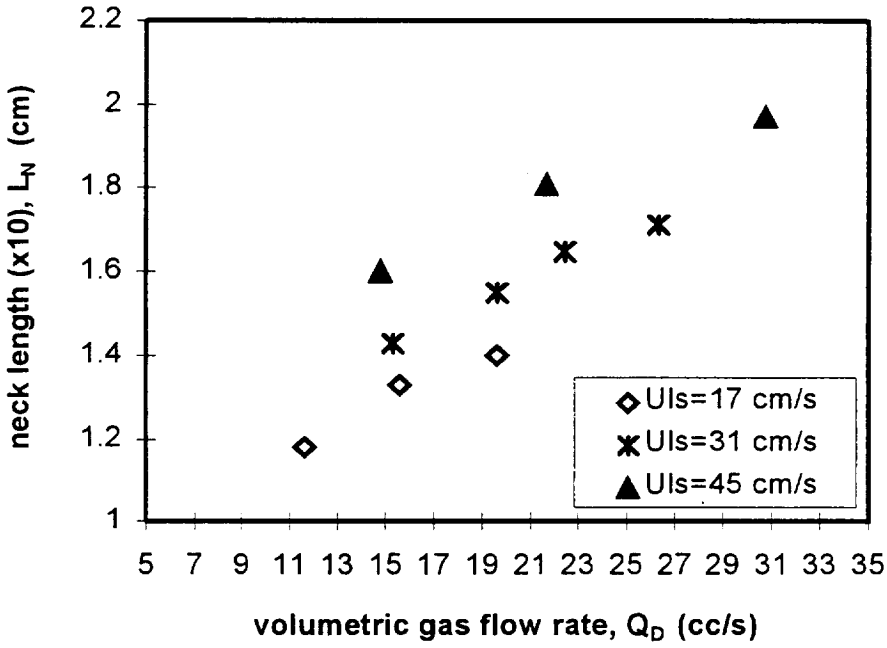

Figure 14. Co-flow configuration: Change of bubble neck length L_N (elongation length, En) as a function of volumetric gas flow rate, Q_d for the $D_P = 1.27$ cm test section ($D_N^* = 0.1$)

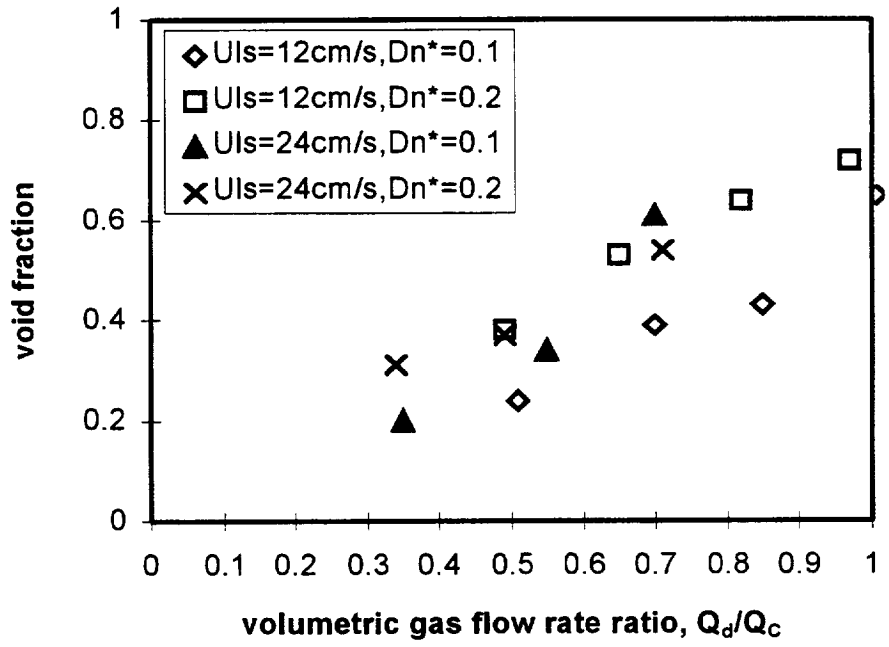

Figure 15. Co-flow configuration: Variation of void fraction ε with respect to Q_d/Q_c for D_N^* = 0.1 and 0.2, D_P =1.9 cm

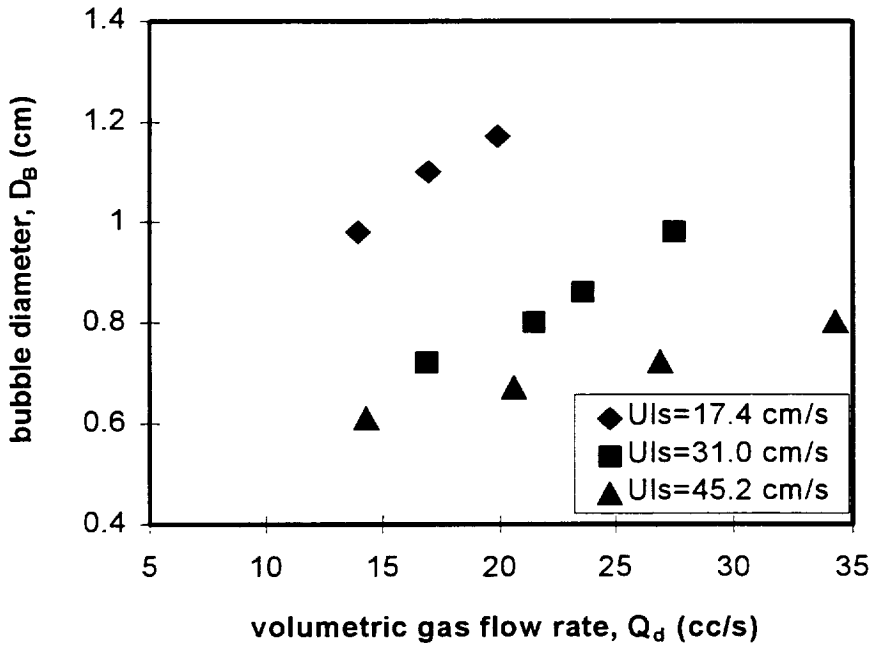

Figure 16. Cross-flow configuration: variation of bubble diameter as a function of Q_d and U_{LS}, for D_P = 1.27cm and D_N^* = 0.1

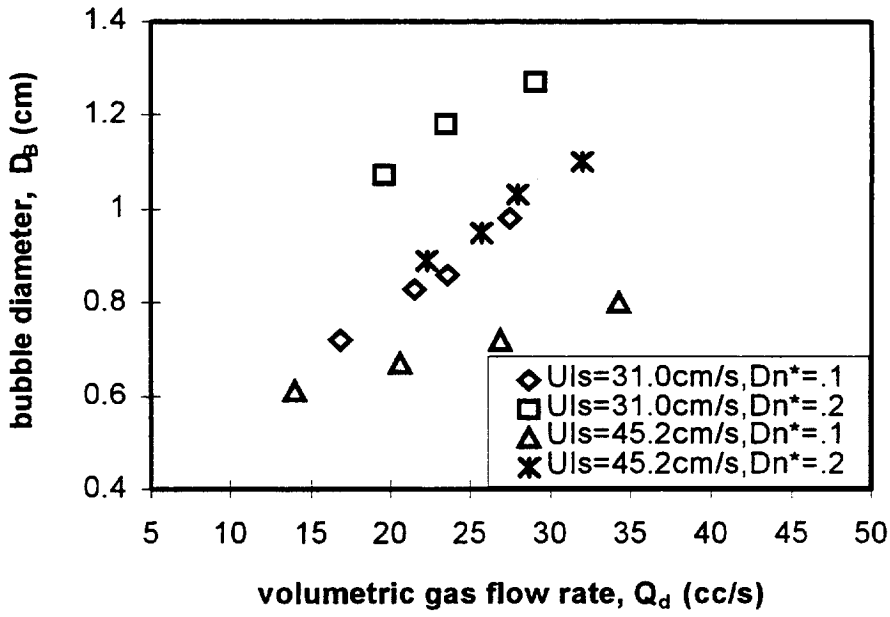

Figure 17. Cross-flow configuration: effect of air injection nozzle diameter aspect ratio on bubble diameter, D_P = 1.27 cm, D_N^* = 0.1 and 0.2

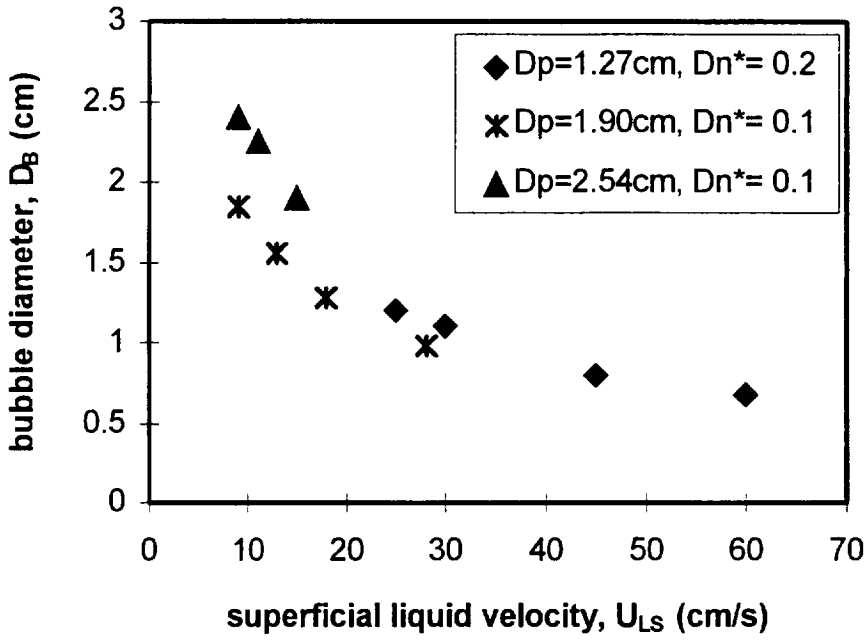

Figure 18. Cross-flow configuration: variation of bubble diameter with respect to superficial liquid velocity for D_P = 1.27 cm, 44 cc/s; D_P = 1.9 cm, Q_d = 28 cc/s and 2.54 cm, D_P = 2.54 cm, Q_d = 61 cc/s test sections

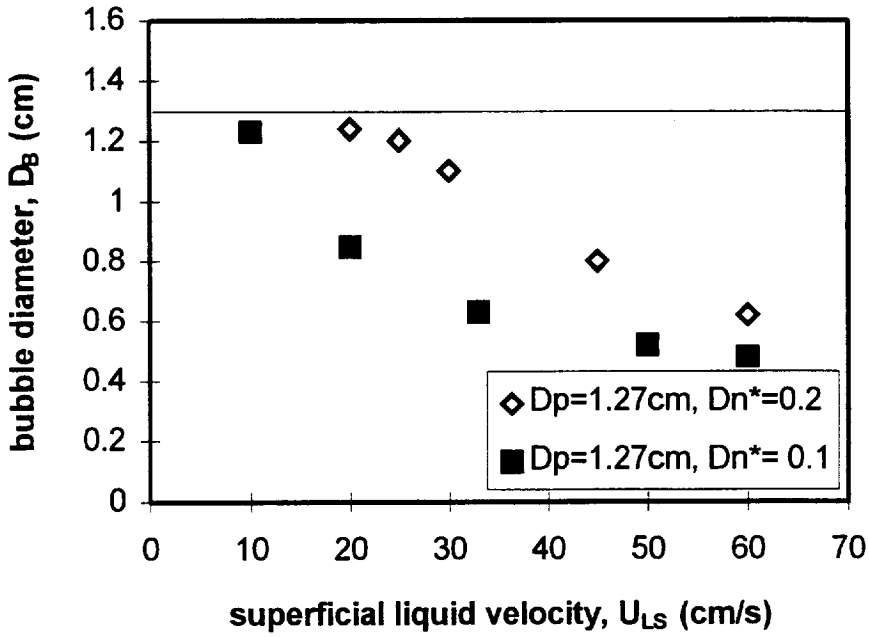

Figure 19. Cross-flow configuration: effect of superficial liquid velocity and nozzle diameter on bubble size for a fixed Q_d = 44 cc/s and D_P = 1.27 cm

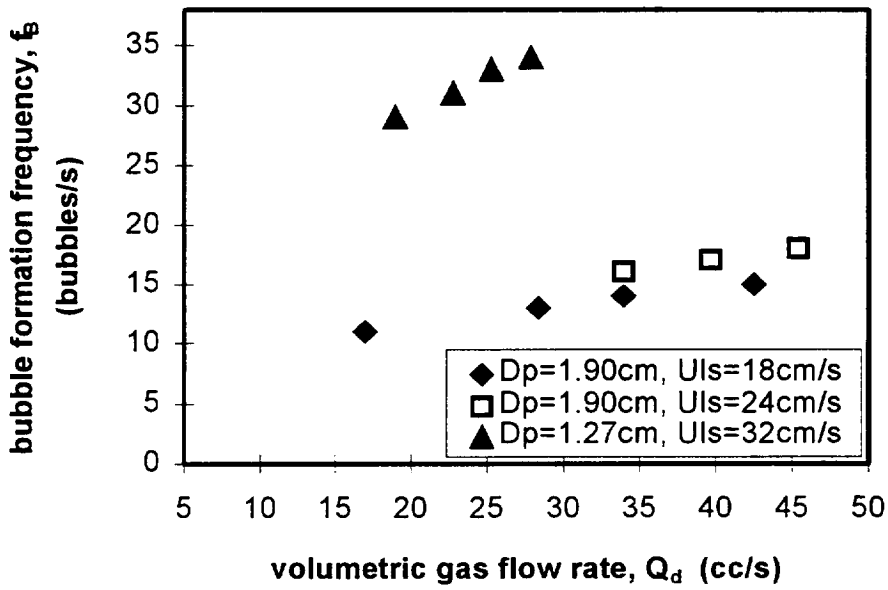

Figure 20. Cross-flow configuration: variation of bubble formation frequency with respect to volumetric gas flow rate, for D_P = 1.27 and 1.9 cm; for D_N^* = .1

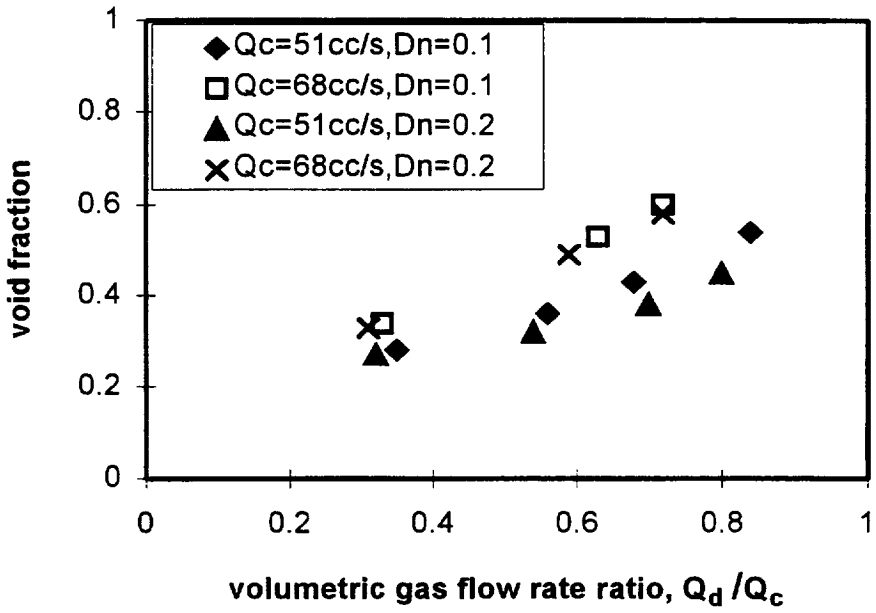

Figure 21. Cross-flow configuration: effect of volumetric gas and liquid flow rates on void fraction with respect to variation in nozzle diameter for a fixed D_P = 1.9 cm

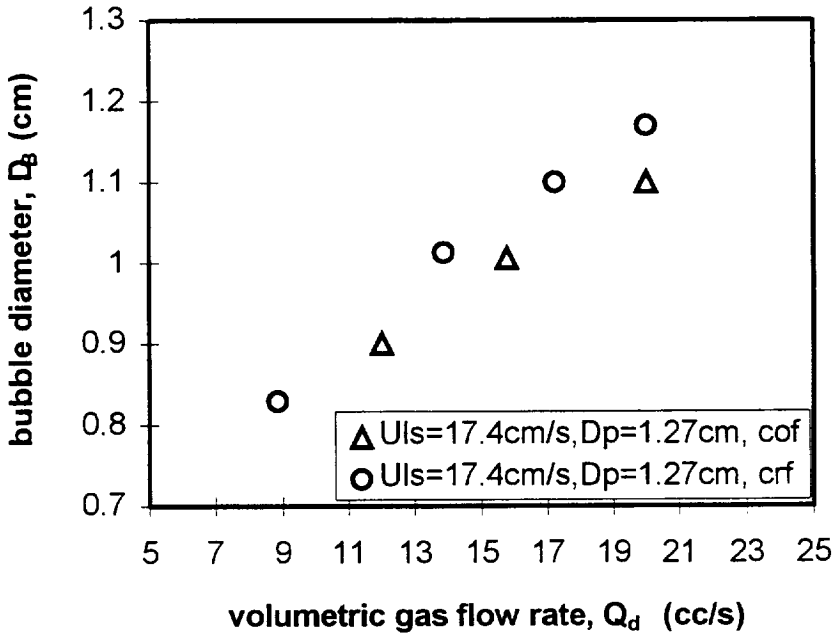

Figure 22. Comparison between empirical values of bubble diameter obtained with the cross-flow system (crf) with those obtained with the co-flow system (cof). Fixed D_P = 1.27 cm and D_N^* = 0.1

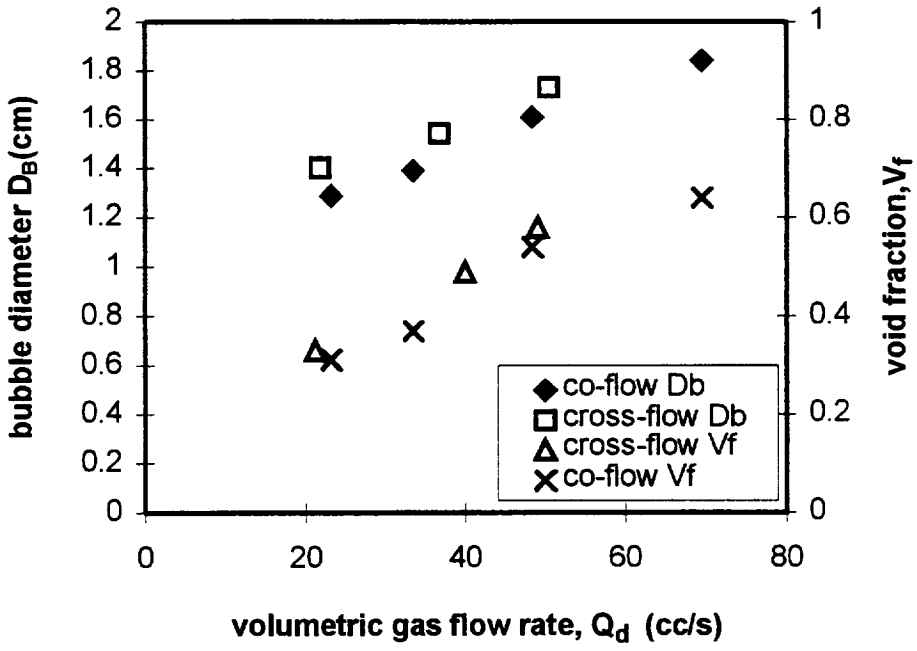

Figure 23. Comparison of bubble diameter and void fraction for the co and cross-flow configurations. Fixed Q_c = 68 cc/s, D_P = 1.9 cm and D_N^* = 0.1

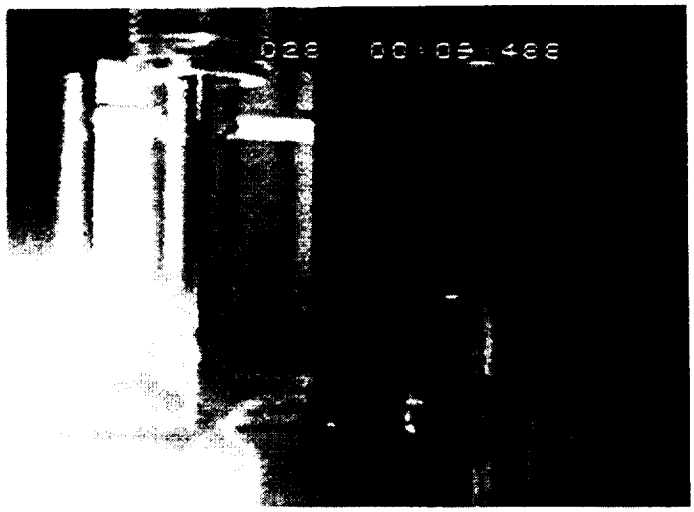

Figure 24. Single video frame of bubble generation in the cross-flow configuration at high liquid and gas volumetric flow rates (U_{LS} = 25 cm/s, Q_d = 76 cc/s, D_P = 1.9 cm, D_N^* = 0.1)

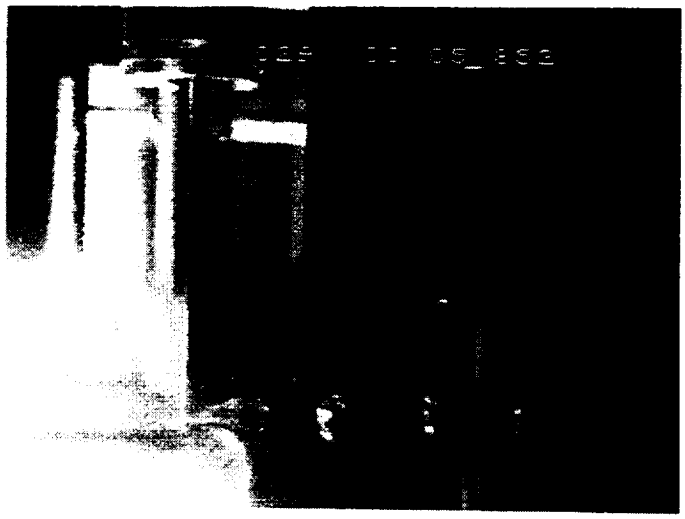

Figure 25. Single video frame of bubble generation in the cross-flow configuration at lower liquid and gas volumetric flow rates than those used in figure 23 (U_{LS} = 15 cm/s, Q_d = 32 cc/s, D_P = 1.9 cm, D_N^* = 0.1)

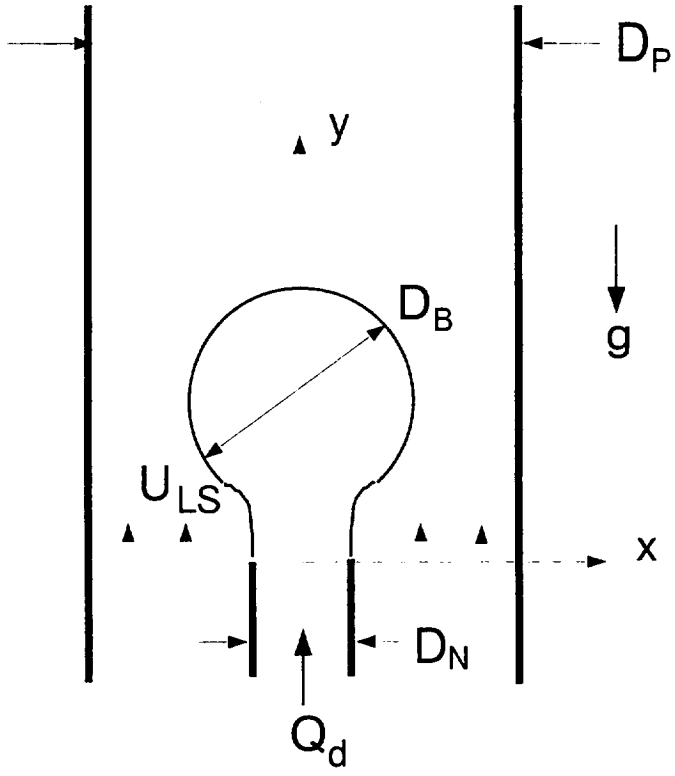

Figure 26. Co-flow configuration used in the Theoretical Model

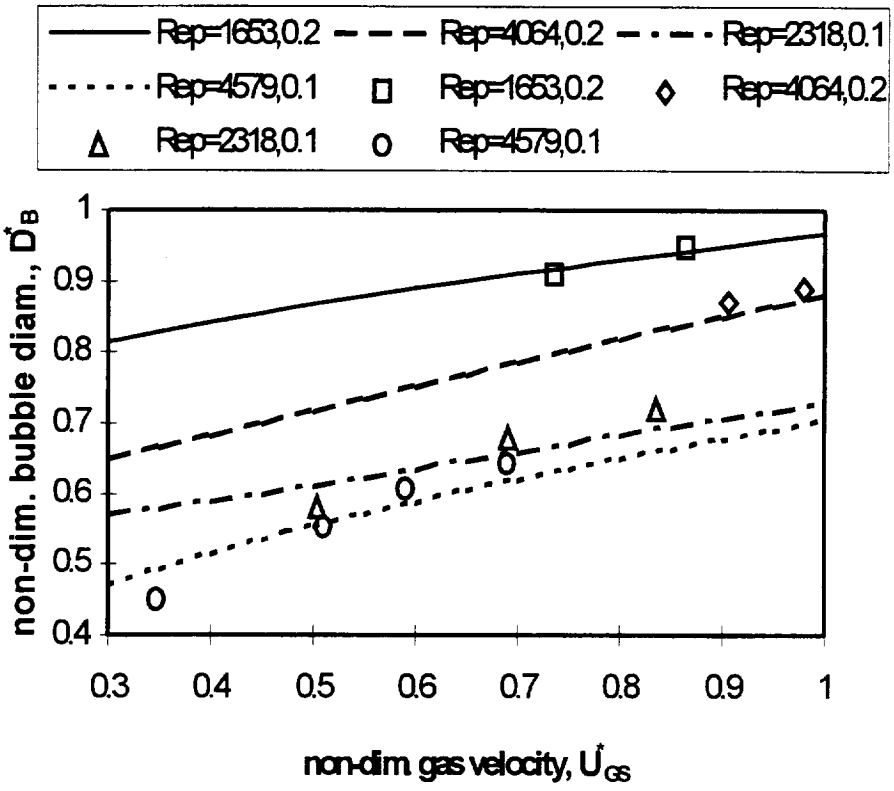

Figure 27. Comparison of bubble diameter empirical values with numerical predictions of bubble size; lines represent computed values, symbols represent empirical values, $D_N^* = .1$ and .2; $\rho^* = 0.0012$; $Re_P = 1653$, $We_P = 1.97$ and $Fr_P = 4.07$; $Re_P = 4064$, $We_P = 8.93$, and $Fr_P = 10.28$; $Re_P = 2318$, $We_P = 3.88$, and $Fr_P = 7.99$; $Re_P = 4579$, $We_P = 15.13$ and $Fr_P = 31.19$

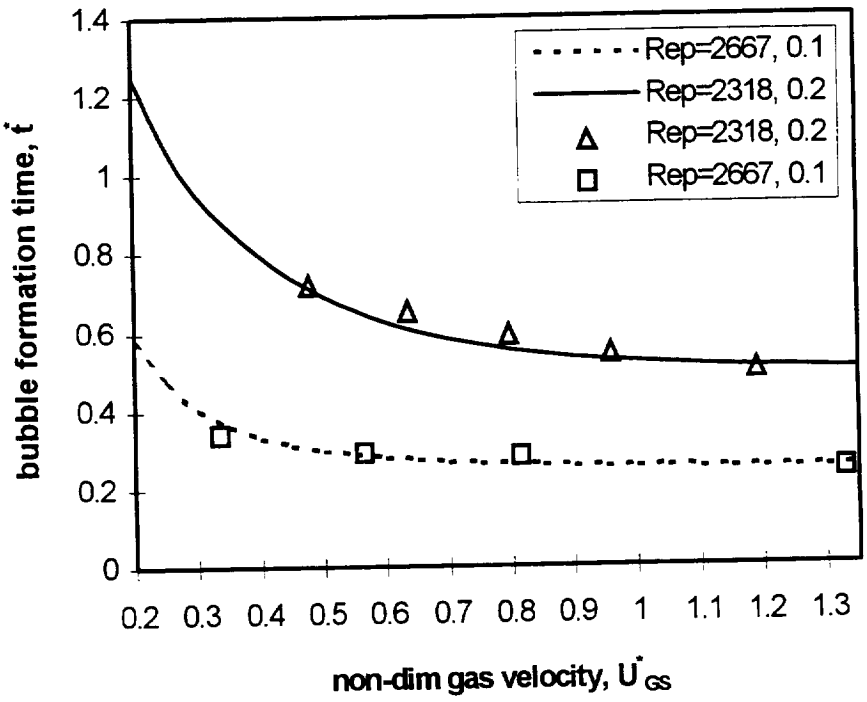

Figure 28. Comparison of numerical and empirical bubble formation time; symbols represent empirical values, lines represent computed values; $D_N^* = 0.1$, $Re_P = 2667$, $We_P = 3.84$ and $Fr_P = 4.43$; $D_N^* = 0.2$, $Re_P = 2318$, $We_P = 3.88$ and $Fr_P = 7.99$

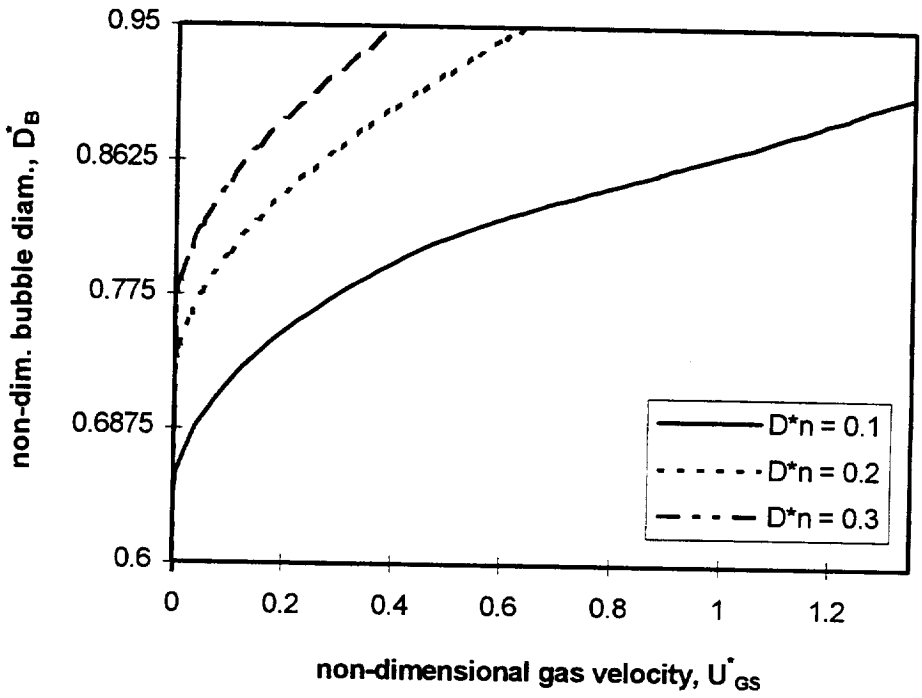

Figure 29. Numerical prediction for variation of bubble diameter with respect to change in superficial gas velocity and gas injection nozzle diameter; $\rho^* = 0.0012$, $Fr_P = 105.25$, $We_P = 0.912$ and $Re_P = 1{,}300$

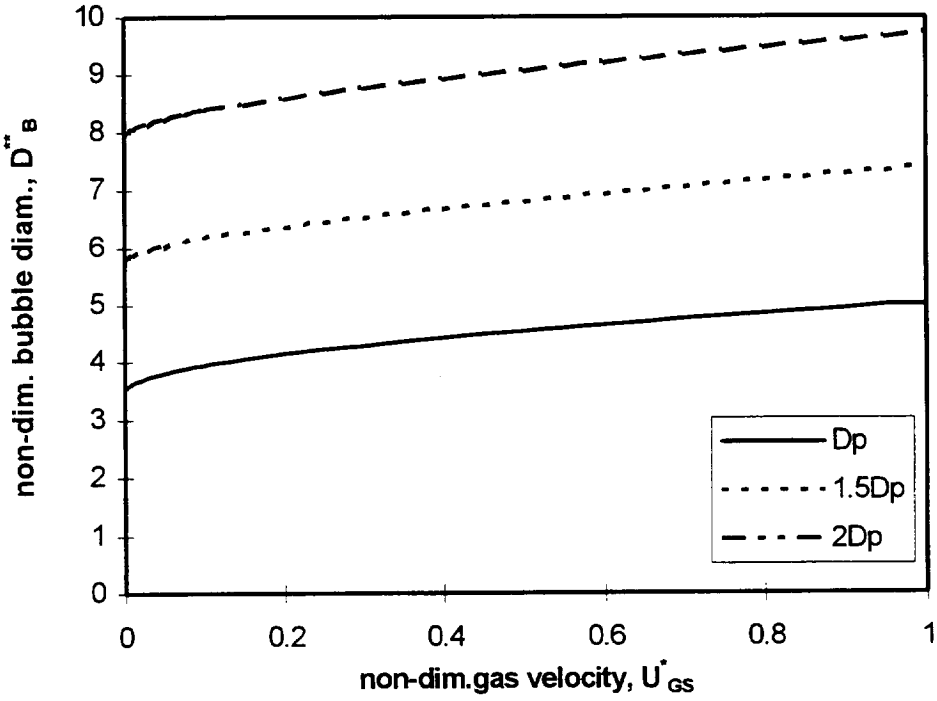

Figure 30. Numerical prediction for the effect of change in pipe diameter on detached bubble diameter $\rho^* = 0.0012$, D_P curve : $D_N^* = 0.20$, $Re_P = 1000$, $We_P = 1.1$, $Fr_P = 498$; 1.5 D_P curve : $D_N^* = 0.133$, $Re_P = 667$, $We_P = 0.32$, $Fr_P = 65.5$; 2 D_P curve : $D_N^* = 0.1$, $Re_P = 500$, $We_P = 0.136$, $Fr_P = 15.5$

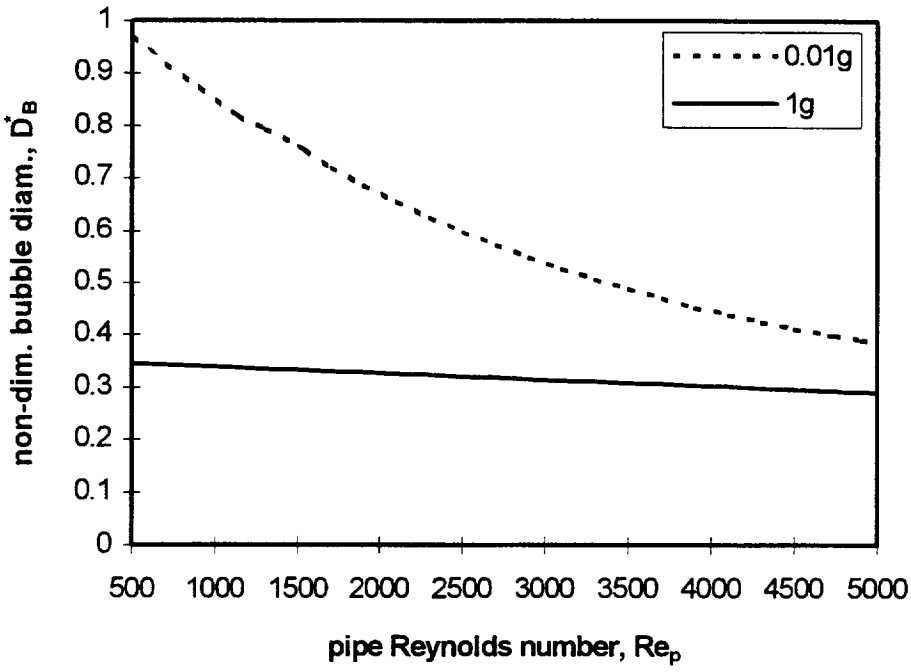

Figure 31. Numerical prediction for the effect of superficial liquid velocity under reduced and normal gravity conditions $\rho^* = 0.0012$, $D_N^* = 0.1$, and $Re_P U_{GS}^* = 500$; 0.01 g curve : $Bo_P = .867$ ($Fr_P = .16$ to 16), 1 g curve: $Bo_P = 86.7$ ($Fr_P = .00016$ to .016)

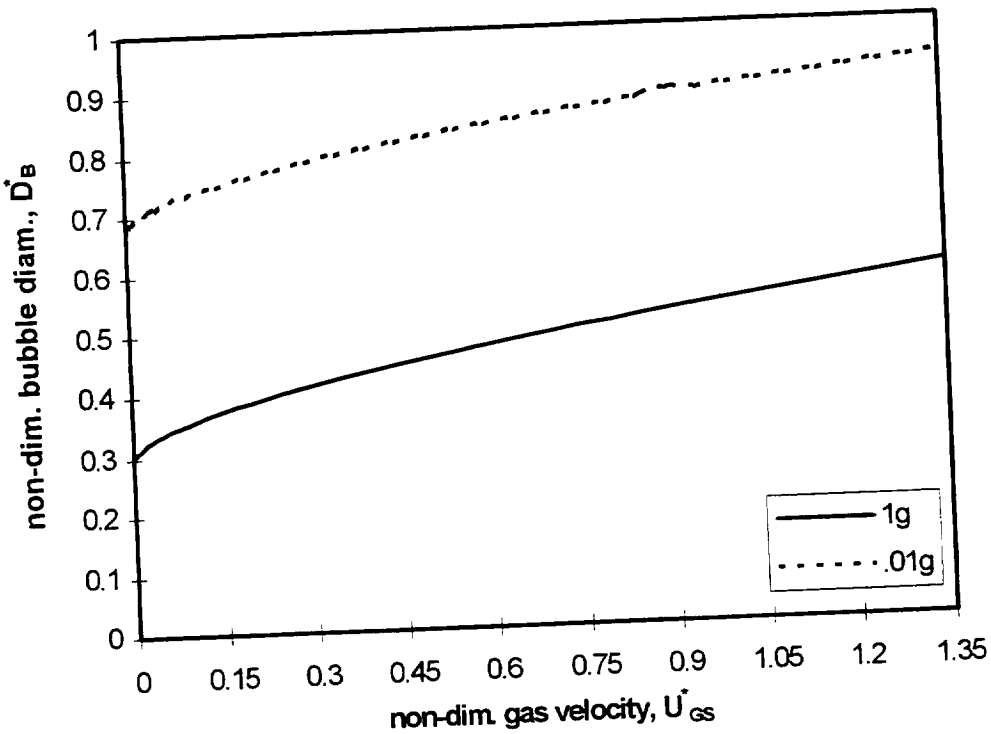

Figure 32. Numerical prediction for the effect of gravity level on bubble diameter; comparison between the reduced gravity and the normal gravity environments $\rho^* = 0.0012$, $D_N^* = 0.1$, $Re_P = 750$, $We_P = .608$; 0.01 g curve: $Fr_P = 2.8$; 1 g curve : $Fr_P = .028$

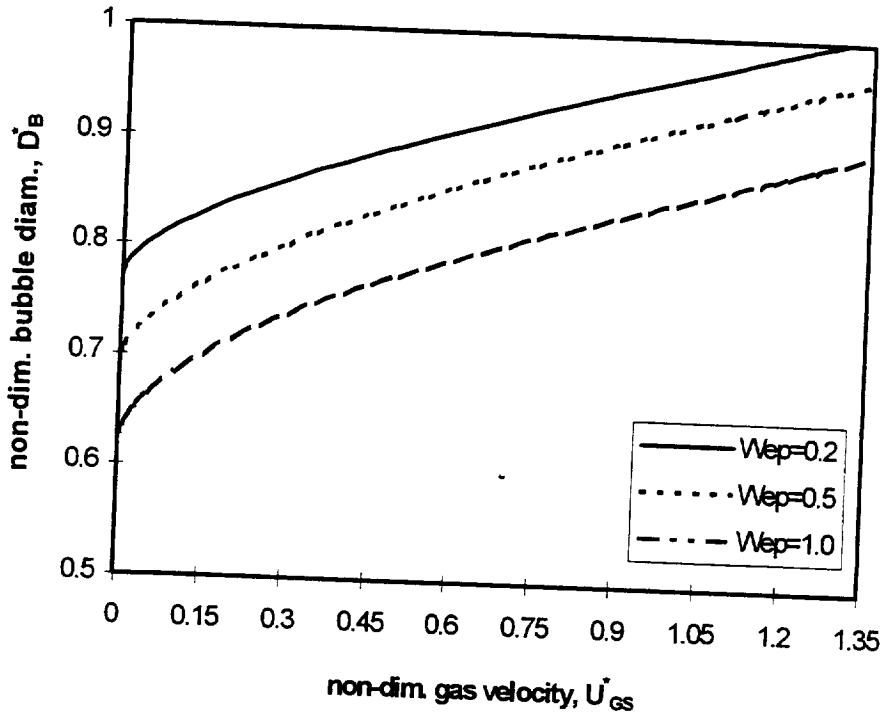

Figure 33. Numerical prediction for the effect of surface tension on detached bubble diameter $\rho^* = 0.0012$, $Fr_P = 22.42$, $Re_P = 600$ and $D_N^* = 0.1$

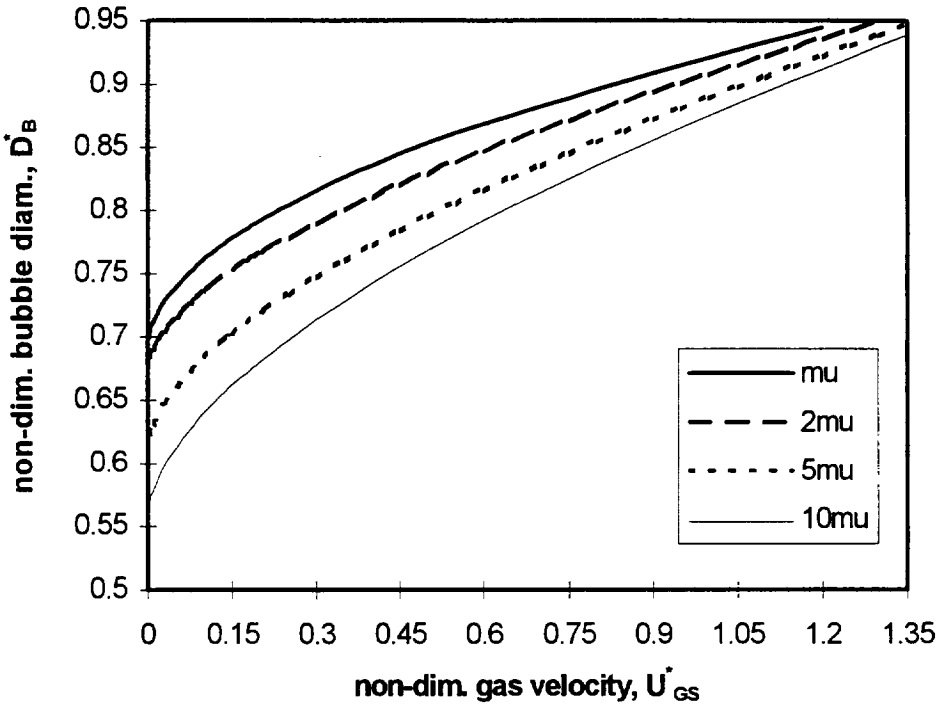

Figure 34. Numerical prediction for the effect of liquid viscosity on detached bubble diameter $\rho^* = 0.0012$, $Fr_P = 62.21$, $We_P = 0.54$ and $D_N^* = 0.1$;"mu" curve : $Re_P = 1{,}000$; 2 "mu" curve : $Re_P = 500$; 5 "mu" curve : $Re_P = 200$ and 10 "mu" curve : $Re_P = 100$

REPORT DOCUMENTATION PAGE

Form Approved
OMB No. 0704-0188

1. AGENCY USE ONLY (*Leave blank*)	2. REPORT DATE	3. REPORT TYPE AND DATES COVERED
	July 1999	Final Contractor Report

4. TITLE AND SUBTITLE

Bubble Generation in a Continuous Liquid Flow Under Reduced Gravity Conditions

5. FUNDING NUMBERS

WU–962–24–00–00
NGT5–1168

6. AUTHOR(S)

Salvatore Cezar Pais

7. PERFORMING ORGANIZATION NAME(S) AND ADDRESS(ES)

Case Western Reserve University
Department of Mechanical Engineering
Cleveland, Ohio 44106–1749

8. PERFORMING ORGANIZATION REPORT NUMBER

E–11771

9. SPONSORING/MONITORING AGENCY NAME(S) AND ADDRESS(ES)

National Aeronautics and Space Administration
John H. Glenn Research Center at Lewis Field
Cleveland, Ohio 44135–3191

10. SPONSORING/MONITORING AGENCY REPORT NUMBER

NASA CR—1999-209170

11. SUPPLEMENTARY NOTES

This report was submitted as a thesis in partial fulfillment of the requirements for the degree Doctor of Philosophy to the Case Western Reserve University, Cleveland, Ohio, August 1998. Project Manager, John B. McQuillen, Microgravity Science Division, NASA Glenn Research Center, organization code 6712, (216) 433–2876.

12a. DISTRIBUTION/AVAILABILITY STATEMENT

Unclassified - Unlimited
Subject Category: 34 Distribution: Nonstandard

This publication is available from the NASA Center for AeroSpace Information, (301) 621–0390.

12b. DISTRIBUTION CODE

13. ABSTRACT (***Maximum 200 words***)

The present work reports a study of bubble generation under reduced gravity conditions for both co-flow and cross-flow configurations. Experiments were performed aboard the DC-9 Reduced Gravity Aircraft at NASA Glenn Research Center, using an air-water system. Three different flow tube diameters were used: 1.27, 1.9, and 2.54 cm. Two different ratios of air injection nozzle to tube diameters were considered: 0.1 and 0.2. Gas and liquid volumetric flow rates were varied from 10 to 200 ml/s. It was experimentally observed that with increasing superficial liquid velocity, the bubbles generated decreased in size. The bubble diameter was shown to increase with increasing air injection nozzle diameters. As the tube diameter was increased, the size of the detached bubbles increased. Likewise, as the superficial liquid velocity was increased, the frequency of bubble formation increased and thus the time to detach forming bubbles decreased. Independent of the flow configuration (for either single nozzle or multiple nozzle gas injection), void fraction and hence flow regime transition can be controlled in a somewhat precise manner by solely varying the gas and liquid volumetric flow rates. On the other hand, it is observed that uniformity of bubble size can be controlled more accurately by using single nozzle gas injection than by using multiple port injection, since this latter system gives rise to unpredictable coalescence of adjacent bubbles. A theoretical model, based on an overall force balance, is employed to study single bubble generation in the dynamic and bubbly flow regime. Under conditions of reduced gravity, the gas momentum flux enhances bubble detachment; however, the surface tension forces at the nozzle tip inhibits bubble detachment. Liquid drag and inertia can act either as attaching or detaching force, depending on the relative velocity of the bubble with respect to the surrounding liquid. Predictions of the theoretical model compare well with performed experiments. However, at higher superficial liquid velocities, the bubble neck length begins to significantly deviate from the value of the air injection nozzle diameter and thus the theory no longer predicts the experiment behavior. Effects of fluid properties, injection geometry and flow conditions on generated bubble size are investigated using the theoretical model. It is shown that bubble diameter is larger in a reduced gravity environment than in a normal gravity environment at similar flow conditions and flow geometry.

14. SUBJECT TERMS

Microgravity; Two phase flow; Bubble

15. NUMBER OF PAGES

156

16. PRICE CODE

A08

17. SECURITY CLASSIFICATION OF REPORT	18. SECURITY CLASSIFICATION OF THIS PAGE	19. SECURITY CLASSIFICATION OF ABSTRACT	20. LIMITATION OF ABSTRACT
Unclassified	Unclassified	Unclassified	